

1 Responses to the editor's comments are in green below each comment. A marked-up version of the revised  
2 manuscript is attached after the responses. Thank you for your time and comments!

3  
4 12: The change in this sentence in response to Reviewer #1 is imprecise. "further spatial and temporal variations in ice  
5 albedo increasingly accentuate the melt regime and recession occurs" is evocative but unclear. The following is more  
6 straightforward: "more dark, bare ice is exposed, decreasing local albedo and increasing surface melting." Because a  
7 link between surface melt and recession is not directly shown in this MS, I recommend setting aside the latter process.

8 Changed as suggested.

9  
10 23: "wish to" is unnecessary

11 Removed "wish to".

12  
13 Table 1 is an especially great addition. Thanks for presenting this history.

14  
15 158, 161: An in review MS should not be cited.

16 Removed the citations of the MS in review and changed to a citation of this data set where appropriate:

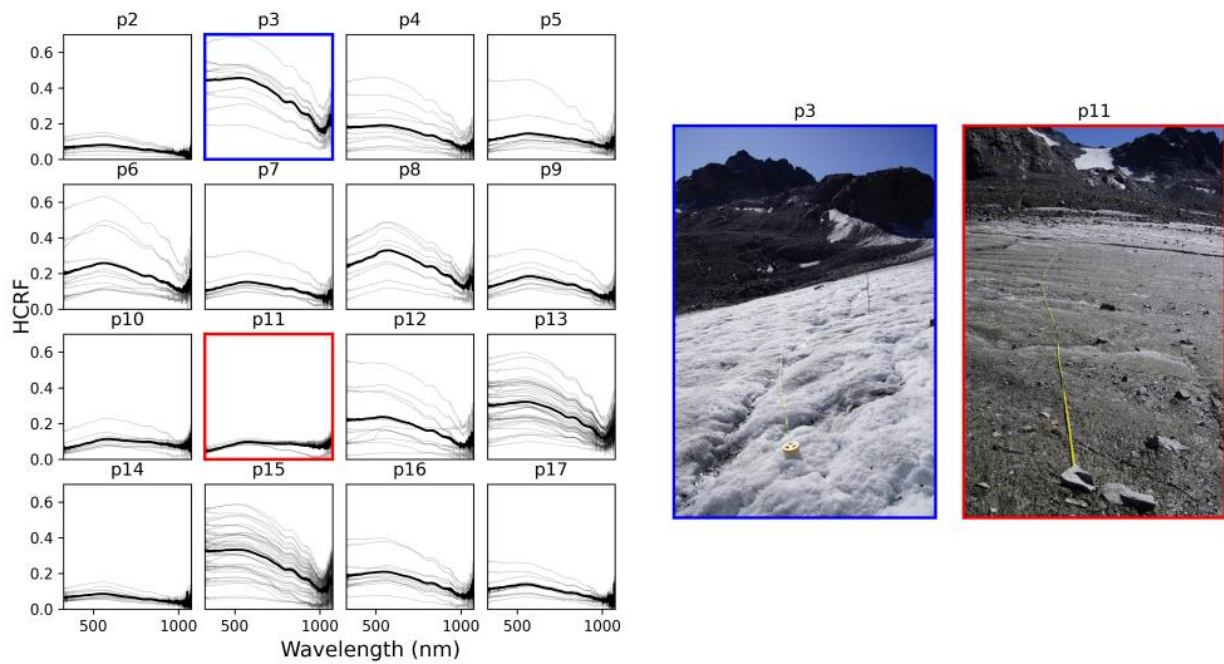
17 Fischer, Andrea; Markl, Gerhard; Kuhn, Michael (2016): Glacier mass balances and elevation zones of Jamtalferner,  
18 Silvretta, Austria, 1988/1989 to 2016/2017. *Institut für Interdisziplinäre Gebirgsforschung der Österreichischen*  
19 *Akademie der Wissenschaften, Innsbruck, PANGAEA, <https://doi.org/10.1594/PANGAEA.818772>*

20  
21 189: "bare fibre optic" Is there a missing word here? Perhaps cable?

22 Changed to: "...a bare fibre optic cable without additional fore-optics".

23 Figures 3/4: I suggest merging these two figures, labeling the photos P3/11, and outlining both their reflectance  
24 spectra and the photos with distinct colors.

25  
26 We have merged the figures and changed the figure numbering throughout the text accordingly. Please indicate if you  
27 were envisioning some other kind of arrangement for the figures, we will adjust as needed.



28

29 Figure 3: Each subplot on the left shows the spectra along a profile line. The bold black lines highlight the mean  
 30 spectral reflectance (HCRF) in each profile. Fotos of the ice surface along p3 and p11 are shown on the right for visual  
 31 context. Fotos were taken at the time of the respective measurements by A. Fischer.

32

33

34 Figure 8: What do the black diamonds signify? Add to legend.

35 The black diamonds are the outliers of the box plot, ie data points that fall outside of 1.5x the interquartile range. We  
 36 changed the symbol from a diamond to a + so that there is less similarity between the outlier symbol and the points  
 37 representing the landsat and sentinel data. We also added the following sentence to the figure caption: The boxes  
 38 represent the first and third quartile. The whiskers represent 1.5x the interquartile range, the + symbols are outliers.

39

40  
41  
42  
43  
44  
45  
46  
47  
48  
49  
50  
51  
52  
53  
54  
55  
56  
57  
58  
59  
60  
61  
62  
63  
64  
65  
66  
67  
68  
69  
70  
71  
72  
73  
74  
75  
76  
77  
78  
79  
80  
81  
82  
83  
84  
85  
86  
87  
88  
89  
90  
91  
92  
93  
94  
95  
96  
97  
98  
99

Small scale spatial variability of bare-ice reflectance at Jamtalferner, Austria

Lea Hartl (1), Lucia Felbauer (1), Gabriele Schwaizer (2), Andrea Fischer (1)

1) Institute for Interdisciplinary Mountain Research, Austrian Academy of Sciences, Technikerstraße, 21a, ICT, 6020 Innsbruck, Austria

2) ENVEO GmbH, Fürstenweg 176, 6020 Innsbruck, Austria

## Abstract

As Alpine glaciers become snow free in summer, ~~further spatial and temporal variations in ice albedo increasingly accentuate the melt regime and recession occurs~~ more dark, bare ice is exposed, decreasing local albedo and increasing surface melting. To include this feedback mechanism in models of future deglaciation, it is important to understand the processes governing broadband and spectral albedo at a local scale. However, little in situ reflectance data has been measured in the ablation zones of mountain glaciers. As a contribution to this knowledge gap, we present spectral reflectance data (Hemispherical-Conical-Reflectance-Factor) from 325 to 1075 nm collected along several profile lines in the ablation zone of Jamtalferner, Austria. Measurements were timed to closely coincide with a Sentinel-2 and Landsat-8 overpass and are compared to the respective ground reflectance (Bottom-Of-Atmosphere) products. The brightest spectra have a maximum reflectance of up to 0.7 and consist of clean, dry ice. In contrast, reflectance does not exceed 0.2 for dark spectra where liquid water and/or fine-grained debris are present. Spectra can roughly be grouped into dry ice, wet ice, and dirt/rocks, although gradations between these groups occur. Neither satellite captures the full range of in situ reflectance values. The difference between ground and satellite data is not uniform across satellite bands, between Landsat and Sentinel, and to some extent between ice surface types (underestimation of reflectance for bright surfaces, overestimation for dark surfaces). We ~~wish to~~ highlight the need for further, systematic measurements of in situ spectral reflectance properties, their variability in time and space, and in-depth analysis of time-synchronous satellite data.

## 1. Introduction

### 1.1 General context and aims

Under ongoing climate change, mountain glaciers are retreating at unprecedented rates (Zemp et al., 2015, 2019). Glaciers in the Eastern Alps are losing mass rapidly, and due to persistent loss of snow cover exposing the underlying firn (Fischer, 2011), many have lost much of their firn cover. An increasing amount of darker bare ice is exposed in Summer and at some glacier tongues, darkening of the ice has been observed (Klok et al., 2003). These feedback mechanisms in turn increase the amount of energy absorbed and accelerate melt (e.g. Paul et al., 2005; Box et al., 2012; Naegeli et al., 2017 & 2019). The reflective properties of glacier ice are affected by e.g. the absence or presence and amount of dust, pollen, debris, cryoconite, supraglacial water, and biota including local production rates (Dumont et al., 2009; Gabbi et al. 2015; Azzoni et al., 2016). Variability is understood to be high, but few measurements and models exist. In a glaciological context, the spatial and temporal variability of ice albedo is understudied compared to snow albedo.

We present spectroradiometric data on the spatial variability of bare-ice reflectance at the tongue of Jamtalferner, Austria, aiming to contribute to closing the knowledge gap in bare ice variability as an important feedback mechanism in glacier mass loss. Specifically, we aim to:

- 1) Provide a first-order quantitative assessment of spatial variability of surface reflectance in the ablation area of the rapidly melting Jamtalferner, quantifying possible ranges of spectral reflectance and qualitatively summarizing different surface types.
- 2) Compare commonly used reflectance products derived from Landsat-8 and Sentinel-2 data with in situ measurements, highlighting areas in which further study is required if ongoing processes related to deglaciation are to be fully captured by satellite data.

### 1.2 In situ and remote sensing-based change detection of surface reflectance properties of glacier ice

In the following section we summarize previous studies on this topic. For clarity, we begin with a note on terminology: Following the definitions and guidelines detailed in Schaepman-Strub et al., (2004, 2006) and Nicodemus et al. (1977), we use the term “albedo” for bihemispherical reflectance (BHR), including cases where this parameter is approximately measured with an albedometer. In situ measurements with field spectrometers – such as they were carried out for this study – generally represent Hemispherical-Conical-Reflectance-Factors (HCRF). For exact specifications of what is represented by satellite derived surface reflectance products we refer to the documentation of the respective products as

100 this differs between sensors and product suites.

101  
102 While it is generally understood that albedo is a major driving factor for the energy balance and radiative regime of  
103 glaciers, few studies discuss ice albedo and its variability at the local level. Early investigations of ice albedo were  
104 carried out by Sauberer in 1938. Building on this work, Sauberer and Dirmhirn (1951) showed that albedo is highly  
105 variable in time and space and strongly affects the radiation balance. They reported mean values of 0.37 for clean ice  
106 and 0.13 for dirty ice at Sonnblick glacier (Austria), a pronounced diurnal cycle of albedo related to refreezing of the  
107 surface, and influence of wind transported fine mineral dust. In another study based on measurements at Sonnblick, they  
108 highlighted that the collection of mineral dust in cryoconite holes affects albedo, as does liquid water, and showed a  
109 diurnal reduction of albedo of about 0.2 under clear sky conditions, which they attribute to melt-freeze cycles on the ice  
110 surface (Sauberer and Dirmhirn, 1952). Jaffé (1960) also pointed out the importance of cryoconite and air content in the  
111 upper most ice layer for the radiative properties. Dirmhirn and Trojer (1955) presented a histogram-like curve of the  
112 frequency of different ice albedo values measured on the tongue of Hintereisferner (Austria): Broadband ice albedo  
113 ranges from <0.1 to about 0.58, with a frequency maximum at 0.28. Similar to the results from Sonnblick, melt-related  
114 diurnal albedo variations were also found at Hintereisferner. In a detailed study of the radiation balance at  
115 Hintereisferner, Hoinkes and Wendler (1968) showed the importance of summer snow falls for albedo, as well as  
116 seasonal changes in ice albedo, and their significant contribution to ablation.

117  
118 Considering the growing dominance of bare ice areas both compared to overall glacier area and in terms of glacier-wide  
119 mass- and energy balance, the sensitivity of the latter parameters to changing reflectance properties has become of  
120 increasing interest throughout approximately the last decade. Using a combination of mass balance data from multiple  
121 Swiss glaciers and the Landsat-8 surface reflectance product, Naegeli and Huss (2015) show that mass balance  
122 decreases on average by 0.14 m w.e. a<sup>-1</sup> per 0.1 albedo decrease. In order to better delineate associated driving  
123 processes at the glacier surface, it is important to assess reflectance properties not only as broadband albedo at the scale  
124 of a glacier, but at a high spectral and spatial resolution. A number of studies attribute recent darkening of European  
125 glaciers to increased accumulation of mineral dust (e.g. Oerlemans et al., 2009, Azzoni et al., 2016) and black carbon  
126 (e.g. Painter et al., 2013, Gabbi et al., 2015). Similar findings have been reported from the Himalayas (e.g. Ming et al.  
127 2012, 2015; Qu et al. 2014) and the Greenland ice sheet (Dumont et al., 2009). Some discussion remains as to whether  
128 the observed darkening is primarily due to the increase of bare ice areas compared to overall glacier area, or whether  
129 there is a darkening of the bare ice areas as such, and if so, whether bare ice areas are darkening due to local processes  
130 or large scale systemic change (e.g. Box et al., 2012; Alexander et al., 2014; Naegeli, 2019).

131  
132 Different methodological approaches have been used to address specific changes in the surface characteristics of the  
133 ablation zone as they relate to changes in reflectance properties and energy absorption across the electromagnetic  
134 spectrum: Using both hyperspectral satellite data and in situ HCRF measurements, Di Mauro et al. (2017) find that the  
135 presence of elemental and organic carbon leads to darkening of the ablation zone at Vadret da Morteratsch (Switzerland)  
136 and discuss potential anthropogenic contributions. Azzoni et al. (2016) use semi-automatic image analysis techniques  
137 on photos of the ice surface at Forni glacier (Italy) to quantify the amount of fine debris present on the surface and its  
138 effect on the albedo. They find an overall darkening due to increasing dust, as well as significant effects of melt and rain  
139 water. Naegeli et al. (2015) use in situ spectrometer and airborne image spectroscopy data with a pixel resolution of  
140 approximately 2m to classify glacier surface types and map spectral albedo on Glacier de la Plaine Morte in  
141 Switzerland. Additionally, they highlight the difference in scale between albedo variability at the ice surface and the  
142 pixel resolution of satellite data and the need for detailed case studies combining ground truth data and remote sensing  
143 techniques to bridge this gap. In situ data is also essential for model verification, as shown e.g. by Malinka et al. (2016),  
144 who use reflectance spectra (HCRF) gathered on sea ice to validate modelled reflectance parameters.

145  
146 In order to scale assessments of ice albedo from the local to a regional or global level, satellite-derived data are  
147 indispensable. Earlier in the satellite era, several studies carried out comparisons of albedo data measured on the ground  
148 and surface reflectance derived from Landsat-5 Thematic Mapper scenes, finding considerable differences between in  
149 situ and satellite data especially in the ablation area (e.g. Hall et al., 1989 & 1990; Koelemeijer et al., 1993; Winther,  
150 1993; Knap et al., 1999). These works are mostly based on albedo data from a single location, such as an automatic  
151 weather station (AWS), and it was often not possible to carry out ground measurements so that they coincided with the  
152 satellite overpasses. More recently, Brun et al. (2015) highlight the importance of remote sensing data for monitoring of  
153 glacier albedo changes in remote regions where data collection on the ground is impossible or impractical and compare  
154 MODIS data with in situ radiation measurements. Albedo measurements from AWS sites on the Greenland ice sheet –  
155 associated with the PROMICE and GC-Net monitoring networks - have been used to improve gridded albedo products  
156 based on MODIS data, showing the importance of using ground truth in conjunction with satellite data (Box et al.,  
157 2013; van As et al., 2017). Narrow-to-broadband conversions remain a challenge in this regard and commonly used  
158 conversions are typically designed for use with Landsat-5 or 7, rather than Landsat-8 or Sentinel-2, which increases the

159 uncertainties inherently associated with any narrow-to-broadband conversion (Gardner et al, 2010; Naegeli et al., 2017).  
 160 In addition, studies assessing the potential effects of anisotropy on satellite-derived surface reflectance data are sparse  
 161 and the magnitude of associated uncertainties is hard to quantify (Naegeli et al., 2015 & 2017).

162 Naegeli et al. (2019) quantify trends in bare ice albedo for 39 Swiss glaciers using Landsat surface reflectance data  
 163 products for a 17-year period. While they do not find a clear, wide spread darkening trend of bare ice surfaces  
 164 throughout the entirety of their data set, they note significant negative trends at the local level, most notably for certain  
 165 terminus areas. A detailed comparison of different albedo products derived from airborne imaging spectroscopy (APEX)  
 166 and Landsat and Sentinel data by Naegeli et al. (2017) further highlights the gap between albedo variability on the  
 167 ground and its representation in remote sensing data of varying resolution. A recent study by Di Mauro et al. (2020)  
 168 uses in situ HCFR data and DNA analysis to show that ice algae affect albedo on a Swiss glacier.

169 Despite the growing body of work on this topic (see Table 1), reflectance properties – spectral as well as broadband,  
 170 local as well as regional, short time as well as seasonal - remain understudied compared to other parameters routinely  
 171 recorded at Jamtalfjerner and other long-term glaciological monitoring sites. However, surface changes and associated  
 172 changes of the spectral characteristics in the ablation area (e.g. due to debris cover, supraglacial meltwater, deposition of  
 173 impurities) are expected to play a significant role in determining the future development of these glaciers. Incorporating  
 174 relevant parameters into monitoring efforts is highly desirable. The accuracy of direct measurements of mass balance  
 175 depends on the representation of all surface types in the stake network, and the correct attribution of unmeasured areas  
 176 to measured stake ablation. Accordingly, a better understanding of how surface types differ in terms of their reflective  
 177 properties is required to maintain the stake network on a rapidly changing glacier. To this end, it is important to  
 178 understand whether satellite-derived data can provide a basis for defining surface classes to be covered by stakes, or  
 179 whether it does not allow for the retrieval of the full bandwidth of reflectance variability relevant to the ice melt rate. In  
 180 addition, delineating the temporal variability of reflectance properties is relevant to degree day modelling, as a changing  
 181 albedo would alter parameters in the model.  
 182  
 183  
 184

Table 1: Measurements of bare ice reflectance properties on mountain glaciers: Overview.

Glacier	Albedo type	Temporal resolution	Spatial resolution	Reference
Hintereisferner, AT	Total	Multiple days	Multiple points on different surface types	Dirmhirn and Trojer, 1955.
Hintereisferner, AT	Total	Multiple times on one day	2 points	Jaffé, 1960.
Northern China (glacier not specified)	Spectral	Not specified	Different surfaces	Zeng et al., 1984.
Forbindels, Greenland	Spectral	One measurement campaign	Regular grid of points around multiple study sites	Hall et al., 1990.
Hintereisferner, AT	Spectral	7 days during ablation season	Points along a profile	Van de Wal et al., 1992.
Austre Brøggerbreen, Midre Lovénbreen, Svalbard	Spectral, total shortwave	Multiple days during ablation season	1 point	Winther, 1993.
Morteratsch, CH	Narrow band (Landsat TM bands 2 and 4)	One measurement campaign	Multiple points	Greuell and de Wildt, 1999.
Haut Glacier d'Arolla, CH	Total	One measurement campaign	Multiple points	Knap et al., 1999.
Hintereisferner, AT	Spectral	One measurement campaign	Multiple points	Hendriksa et al., 2003
Morteratsch, CH	Total	Continuous AWS measurements	Multiple AWS locations	Klok et al., 2003
Chhota Shigri, Mera Glaciers, Nepal	Total shortwave	Continuous AWS measurements	AWS location	Brun et al., 2015.
Forni Glacier, IT	Total	Multiple measurements during multiple years	Multiple points	Azzoni et al., 2016.

Glacier de la Plaine Morte, CH	Spectral	One measurement campaign	Multiple points	Naegeli et al., 2015.
Findelen, CH	Total	Continuous AWS measurements	AWS location	Naegeli et al., 2017.
Morteratsch, CH	Spectral	One measurement campaign	Multiple points	Di Mauro et al., 2017; Di Mauro et al, 2020
Greenland ice sheet	Total	Continuous AWS measurements	Multiple AWS locations	van As et al., 2017; Box et al., 2013
De Geerfonna and Elfenbeinbreen, Svalbard	Total	Continuous AWS measurements	1 AWS on each glacier	Möller and Möller, 2017
Jamtal, AT	Spectral	One measurement campaign	Multiple points	This study

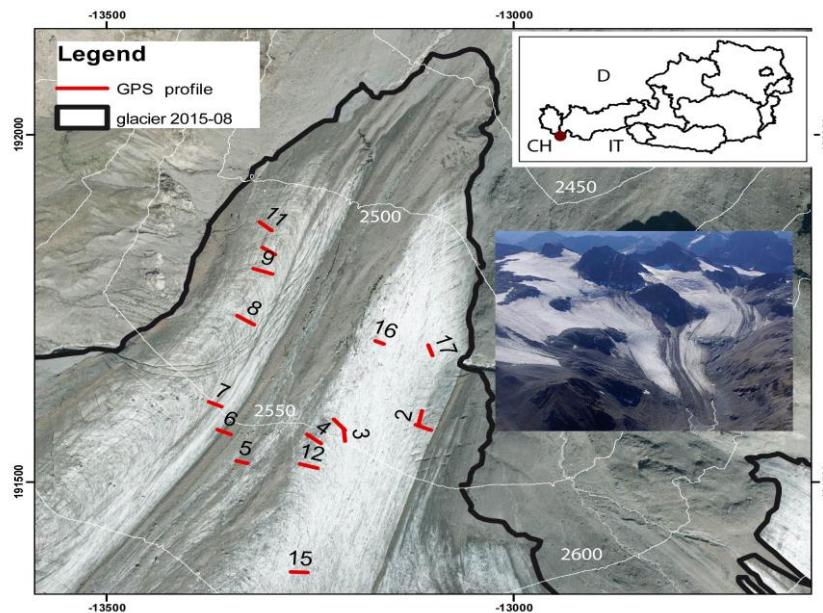
186  
187  
188  
189  
190  
191  
192  
193  
194  
195  
196  
197  
198  
199  
200  
201  
202  
203  
204  
205  
206  
207

## 2. Data, Methods, and Study Site

### 2.1. Study site – glaciological background

Jamtalferner was chosen for this study as it has the smallest end-of-season snow cover amongst the glaciers with long term mass balance monitoring in Austria. Jamtalferner is located in the Silvretta mountain range, which intersects the border between Austria and Switzerland. Jamtalferner is the largest glacier on the Austrian side of Silvretta (Fig. 1, size in 1970: 4.115km<sup>2</sup>, size in 2015: 2.818km<sup>2</sup>). The history of scientific research at the site goes back as far as 1892, when length change measurements were first carried out, and a wealth of cartographic, geodetic, and glaciological data are available (Fischer et al., 2019). Orthophotos and cartographic analysis show that debris cover at the glacier terminus and in the lower elevation zones has increased (debris covered percentage of total area: 1.7% in 1970, 24.1% in 2015), while firn cover is decreasing (firn covered area in 1970: 75%, in 2015: 13%, mean accumulation area ratio (AAR) 1990/91-99/00: 0.35, mean AAR 2010-2017/18: 0.12, Fischer et al., 2016 *in review*).

Mass balance measurements via the direct glaciological method began in 1988/1989. In recent years, increasing mass loss was recorded across all elevation zones (Fischer et al., 2016; Fischer et al., *in review*). The lowest elevation zones are dominant in terms of total ablation and thus net balance. Melt in the lowest altitudes has been increasing during the last two decades of negative mass balances and the variability of surface albedo at and near the glacier terminus affects melt over the full duration of the ablation season.



208 Figure 1: Tongue of Jamtalferner glacier (Orthophoto, August 2015, Source: Tyrolean Government/ TIRIS) with profile  
209 lines of spectrodiometer measurements indicated in red. Insert: Aerial photograph of Jamtalferner, 20.09.2018 (Photo:  
210 Andrea Fischer).  
211  
212  
213

### 2.2 In situ measurements of spectral reflectance

214  
215  
216 The field campaign was carried out on September 4<sup>th</sup>, 2019. This date was selected for two reasons: Favourable weather  
217 conditions and temporal proximity to overpasses of both Sentinel-2 (on the same day) and Landsat-8 (on September  
218 3<sup>rd</sup>). With a large area of high pressure over western and central Europe, the weather at the study site was sunny and dry  
219 on throughout Sept. 3<sup>rd</sup> and 4<sup>th</sup>. Using an ASD Field Spec Handheld 2 spectroradiometer (ASD Inc., 2010), a total of  
220 246 reflectance spectra (HCFR) was collected, with 12 spectra measured at point locations and 234 spectra measured  
221 along 16 profile lines. Profiles were measured along a 20m measuring tape in such a way that individual spectra were  
222 gathered at equal intervals, with 14 profile lines containing 11 spectra spaced at 2 m. 2 profiles contain 40 spectra –  
223 these were also gathered at equal intervals but with a higher resolution. Measurements began at 08:28 GMT (10:28 local  
224 time) and ended at 13:43 GMT. The coordinates of the start and end points of each profile line, as well as any spectra

225 measured outside of the lines, were recorded with a Garmin etrex VISTA HCx, a standard handheld GPS device, which  
226 also recorded the time of day. The horizontal accuracy of the GPS coordinates is better than 3 m as per the internal  
227 accuracy assessment of the GPS device. The timestamps of the GPS points for the start and end points of the profiles  
228 were used to compute solar elevation and azimuth. For each profile, the mean solar elevation and azimuth between the  
229 respective start and end points is given in Table 2. Measurements were taken 35 cm above ground from nadir with a  
230 bare fibre optic cable without additional fore-optics. Test measurements in the field showed high consistency between  
231 multiple measurements at the same point, so that we chose to use single measurements at each location rather than  
232 average over multiple measurements. The instrument was handheld and not mounted on a stand to minimize shading.  
233 This measurement set up is similar to that of previous studies (Naegeli, 2015; Di Mauro et al., 2017) and yields a  
234 circular field of view (FOV) with a radius of approximately 7.8 cm for flat ground. The instrument operates between  
235 325 and 1075 nm with an accuracy of  $\pm 1$  nm and a resolution of  $< 3$  nm at 700 nm. We used a feature of the instrument  
236 that allows the user to save the white reference measurement to the RAM of the built-in computer. HCFR is computed  
237 for subsequent target reflectance measurements based on the saved reference. This is saved to the output file,  
238 eliminating the need to calibrate the target measurements to the white reference in post-processing. A new SRT-99-020  
239 Spectralon (serial number 99AA08-0918-1593) manufactured by Lab Sphere was used for the measurement of the  
240 white reference. The ASD data files were imported into a python script for further analysis using the Python module  
241 SpecDal (Lee, 2017) to read the ASD format. Further data analysis was carried out using numerous other Python (Van  
242 Rossum and Drake., 2009) packages, mainly NumPy (van der Walt et al., 2011), pandas (McKinney, 2010), Matplotlib  
243 (Hunter, 2007), Rasterio (Gillies et al., 2013), GeoPandas (GeoPandas developers, 2019), rasterstats (Perry, 2015), and  
244 PyEphem (Rhodes, 2020).

245  
246

### 247 2.3 Satellite data

248

249 We compare the in situ measurements with surface reflectance products derived from a Landsat-8 Operational Land  
250 Imager (OLI) scene acquired on September 3<sup>rd</sup>, 2019 (10:10 GMT), the day before the field campaign, and a Sentinel  
251 2A scene acquired on September 4<sup>th</sup> (10:20 GMT), the same day as the field campaign. Both scenes are cloud free over  
252 the study area (Figure 2). Details on the atmospheric correction algorithm used to generate the Landsat-8 OLI level-2  
253 surface reflectance data product from top of atmosphere (TOA) reflectance can be found in Vermote et al. (2016) and in  
254 the product guide of the algorithm used to derive surface reflectance (USGS, 2020). Details on the equivalent Sentinel-2  
255 product – the Level-2A bottom of atmosphere reflectance – are given in Main-Knorn et al. (2017) and Richter and  
256 Schläpfer (2011). For the sake of readability, we refer to the Landsat-8 OLI level-2 surface reflectance as “Landsat”  
257 data in the following, and to the Sentinel-2 level-2A surface reflectance as “Sentinel” data. The Landsat and Sentinel  
258 surface reflectance raster data used in this study were acquired using Google Earth Engine (Gorelick et al., 2017).

259

260 The wavelength range of the spectroradiometric measurements carried out on the ground overlaps with bands 1-5 of the  
261 Landsat data and bands 1-9 and 8A of the Sentinel data, respectively. Only spectral ranges covered by these bands are  
262 considered for this study. The wavelengths and resolution of the individual bands, as well as the relevant viewing and  
263 solar angles are given in Table 3. For each ground measurement point, band values were extracted from the satellite  
264 scenes at the overlaying pixel.

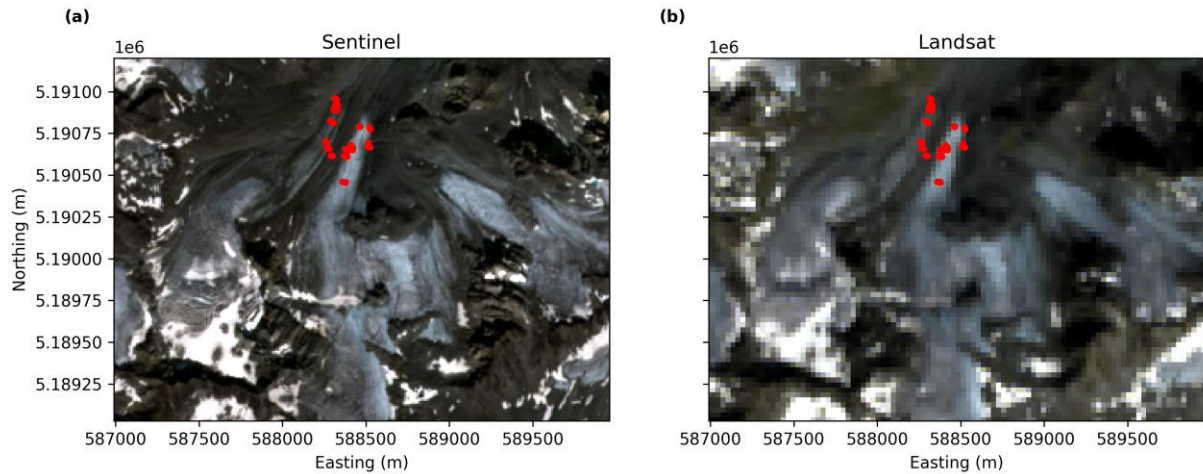
265

266 In order to compare the satellite values with ground data, we compute mean values for the subsets of the spectral  
267 reflectance curves measured on the ground that correspond to the Landsat and Sentinel bands, respectively. Data are  
268 then grouped into profile lines and/or different bands, the Pearson correlation is computed for ground- and  
269 corresponding satellite data, and further comparisons are carried out using standard statistical metrics.

270

271 To assess the influence of the spatial resolution of the satellite data on results, band 3 imagery was resampled (cubic  
272 interpolation) from the original 10 m resolution to 30 m and 60 m for Sentinel and from 30 m to 60 m for Landsat,  
273 respectively. To account for the potential effects of the uncertainty in the GPS coordinates, we created a circular buffer  
274 with a radius of 3m around each in situ measurement point. For each buffer, the corresponding satellite value is  
275 computed as the median of the values of all pixels the buffer overlaps with.



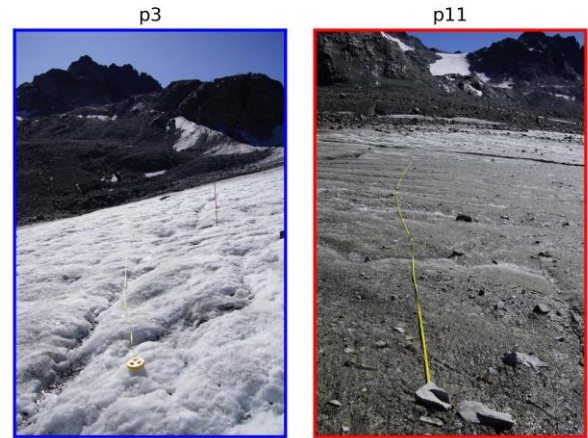
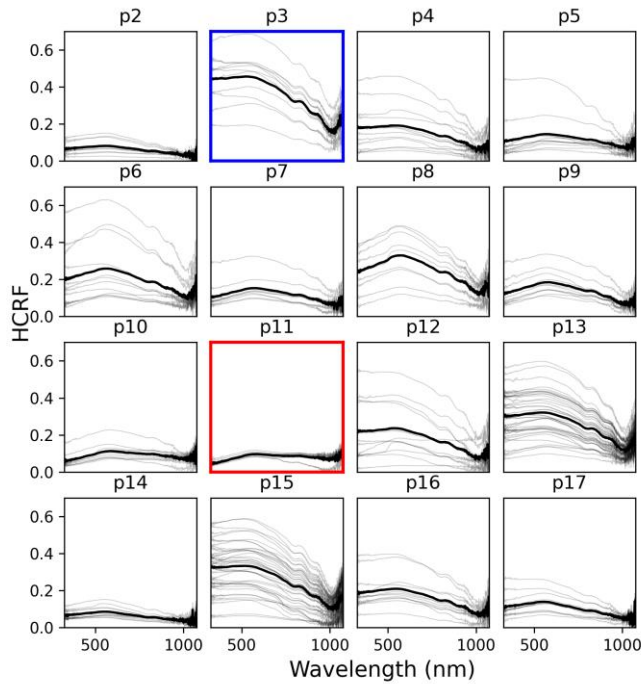


276  
 277 Figure 2: Jamtalferner as seen in the Sentinel (a) and Landsat (b) scenes used in this study. The images shown here are  
 278 composites of bands 2, 3, and 4 of each satellite's L2A surface reflectance product displayed at a resolution of 10  
 279 (Sentinel) and 30 (Landsat) m/pixel, respectively. Profiles where reflectance spectra were collected are marked in red.  
 280 Coordinate reference system: EPSG: 32632.

281  
 282 **3. Results**

283  
 284 **3.1 Surface measurements**

285  
 286 The in situ measurements exhibit extreme differences in HCFR depending on the characteristics of the surface. Figure 3  
 287 shows the spectra grouped into profiles, with the mean spectral HCFR highlighted for each profile. P3 is the "brightest"  
 288 profile, with the highest maximum (up to 0.7) and minimum (up to 0.2) values of all profiles. Profiles 2, 11, and 14 are  
 289 the darkest profiles and all of their respective spectral reflectance remain below 0.2 at all measured wavelengths. Figure  
 290 [3 also](#) shows the ice surface along profile lines 3 (brightest) and 11 (darkest) for a visual comparison. In P3, the  
 291 surface is mainly comprised of clean, dry ice. In P11, the ice surface is wet and impurities (rocks, fine grained debris)  
 292 are present. The profile line crosses several small melt water channels with running water.  
 293



294  
295

Figure 3: Each subplot on the left shows the spectra along a profile line. The bold black lines highlight the mean spectral reflectance (HCRF) in each profile. Fotos of the ice surface along p3 and p11 are shown on the right for visual context. Fotos were taken at the time of the respective measurements by A. Fischer.

298  
299

300  
301

Table 2 contains a qualitative description of the ice surface along each profile line, the length of the line, the number of spectra per line, and the number of Landsat and Sentinel band 3 pixels that each line crosses, as well as the mean solar elevation and azimuth angles for the profile. The maximum number of pixels per line is 5 for Sentinel and 3 for Landsat, respectively. All lines cross at least 2 pixels for Sentinel, while 3 lines fall into a single Landsat pixel. See Fig. 1 for the location of each profile on the glacier.

306  
307

Table 2: Description of the surface characteristics along each profile line, as well as number of spectra collected along the line and number of pixels intersected by the line in band 3 of the Sentinel and Landsat scenes, respectively.

308  
309

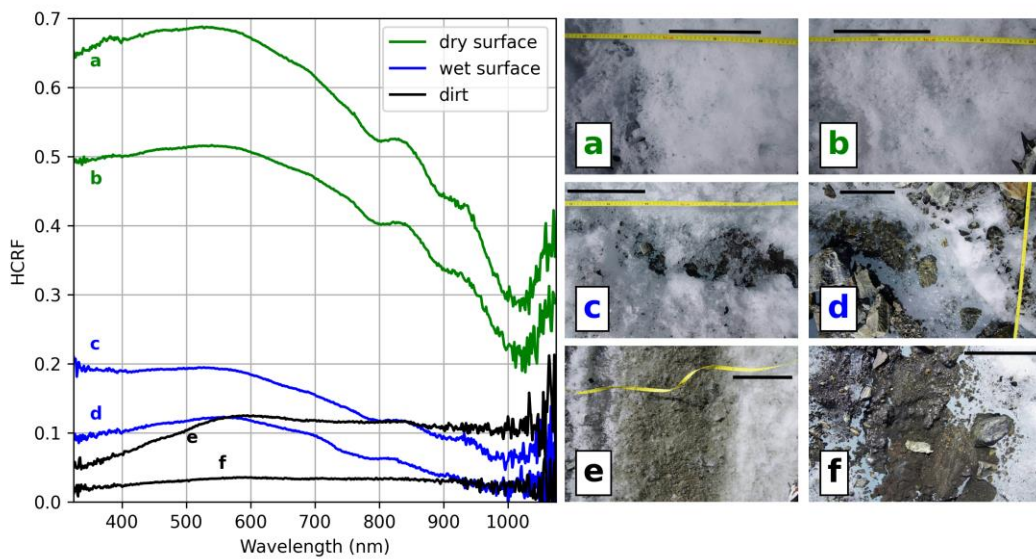
Profile Nr.	Qualitative description	Mean solar elevation, azimuth in degrees	Spectra	Sentinel B3 pixels	Landsat B3 pixels
P2	Relatively smooth, uniform ice surface, slightly wet.	24.69, 106.70	11	3	2
P3	Mostly dry surface, clean cryoconite.	26.43, 108.92	11	4	1
P4	Mostly dry ice surface, some dirt, some rocks/debris on ice surface where profile approaches moraine.	28.64, 111.87	11	4	2
P5	Significant debris cover along profile. Where ice is exposed, ice surface is wet. Profile crosses meltwater channels with running water.	31.34, 115.72	11	3	1
P6	Wet ice surface with dust/dirt transitions to cleaner, brighter ice.	34.45, 120.61	11	4	1
P7	Grey-ish ice surface with meltwater channels and fine-grained debris/small rocks.	36.20, 123.57	11	2	2
P8	Similar to P7, fewer rocks.	38.05, 126.99	11	4	2
P9	Wet ice surface with mixture of relatively clean cryoconite and more dusty areas.	39.40, 129.68	11	3	2
P10	Wet ice surface with several small melt water channels. Mostly dirty, grey ice.	40.71, 132.51	11	3	2
P11	Wet ice surface with several small meltwater channels. Very dirty ice with scattered small rocks.	42.08, 135.75	11	4	2

<b>P12</b>	Relatively clean, bright ice interspersed with larger meltwater ponds/channels, which contain dirt and small rocks.	47.61, 153.83	11	4	3
<b>P13</b>	Clean cryoconite with some darker patches.	48.63, 159.14	40	5	2
<b>P14</b>	Wet ice surface with fine grained dirt in relatively uniform cryoconite.	49.80, 168.30	11	4	2
<b>P15</b>	Uneven ice surface, mostly clean, dry ice.	50.30, 179.29	40	3	2
<b>P16</b>	Mixture of wet and dry ice surface and fine-grained dirt.	49.43, 194.99	11	3	2
<b>P17</b>	Mostly wet ice surface, fine grained dirt with some cleaner patches.	48.33, 202.34	11	2	2

310  
311  
312  
313  
314  
315  
316  
317  
318  
319  
320  
321  
322  
323  
324  
325  
326

The spectral reflectance curves of the individual spectra as well as of the profile lines indicate high spatial variation of surface types and associated reflective properties. The spectral signatures of the individual spectra can roughly be grouped into dry ice, wet ice, and dirt/rocks. (We use the word “dirt” to describe all types of mineral or organic materials and fine-grained debris that may collect on the glacier surface.) However, transitions between these types are gradational and in practice these categories cannot always be clearly separated - both dry and wet ice might be clean or dirty, dirt might be wet or dry.

The reflectance curves for clean ice exhibit the typical shape frequently found in literature (Zeng et al., 1984), with highest reflectance values (up to 0.69) in the lower third of our wavelength range and declining values for wavelengths greater than approximately 580 nm. The spectral reflectance curves of wet ice surfaces follow roughly the same shape as for dry ice but are strongly dampened in amplitude with reflectance values typically not exceeding 0.2. In contrast, the reflectance curve of dirty surfaces remains at uniformly low values throughout our wavelength range in some cases and exhibits an increase between 325 and approximately 550 nm before flattening out in other cases. Reflectance values have similar magnitudes as for wet ice. Example reflectance curves of these surface types are given in Fig. 45.



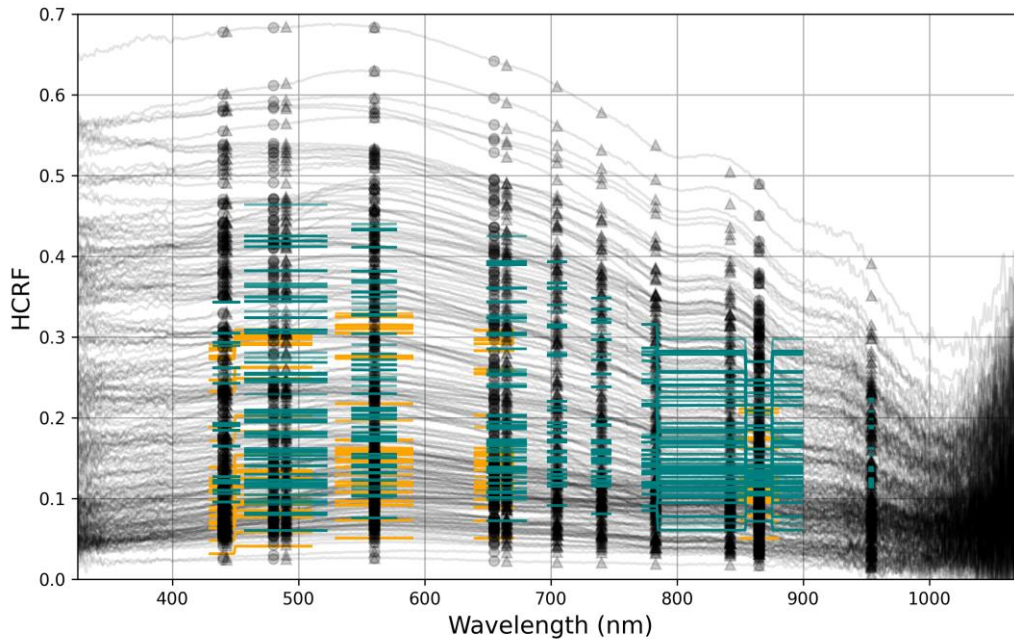
327  
328  
329  
330  
331  
332  
333  
334  
335  
336  
337  
338  
339

Figure 45: Spectra of different kinds of ice surface types encountered in the ablation zone of Jamtalferner. The photos on the right show the ice surface at the sampling sites of the respective spectra. The black bar in each photo represents approximately 20 cm, to provide a sense of scale. The spectra shown in this figure are part of the following profile lines: a, b, c – p3; d – p4; e – p6; f – p12.

### 3.2 Comparison with satellite data

Figure 56 shows all measured spectral reflectance curves, as well as the Sentinel and Landsat values in the bands that overlap the wavelength range of the ground measurements. Reflectance values were extracted from the satellite imagery at the coordinates of each sampling point and overlaid onto the plots of the in situ spectra as coloured bars. Naturally, neither satellite captures the full range of reflectance values measured on the ground. In all overlapping bands of

340 Sentinel and Landsat, the Sentinel values are higher, in the sense that the maximum values of the Sentinel data are  
 341 closer to the maximum values measured on the ground, while the minimum Landsat data are closer to the minimum  
 342 values measured on the ground.  
 343



344  
 345  
 346 Figure 56: The spectra measured in situ are plotted in black. Black circles indicate the central wavelengths of the  
 347 Landsat bands, black triangles those of the Sentinel bands (see Table 3). Orange and blue lines represent the wavelength  
 348 range of the respective Landsat and Sentinel bands along the horizontal axis and the satellite derived reflectance at the  
 349 sampling points of each spectrum on the vertical axis.  
 350

351 Comparing the mean of the HCRF spectra measured on the ground for each satellite band with the associated satellite  
 352 values yields a Pearson correlation coefficient ranging from 0.53 (band 5) to 0.62 (band 1) for the Landsat bands and  
 353 0.3 (band 9) to 0.65 (band 2) for Sentinel. Table 3 lists the correlation coefficients, as well as the wavelength range and  
 354 resolution of each band. The two lower resolution Sentinel bands (band 1, band 9 – 60m resolution) have notably lower  
 355 correlation coefficients than the higher resolution bands. The Sentinel and Landsat data at the in situ measurement  
 356 points are strongly correlated with each other in the bands where both satellites overlap, with  $r=0.69$  in band 1 and  $r>0.8$   
 357 for bands 2, 3, 4, and 5.  
 358

359 For a visual comparison of the location of the profile lines and the range of measured values in the profiles in relation to  
 360 the satellite pixel boundaries and pixel band values, see Fig. 67 for Sentinel (band 3 selected as an example) and  
 361 supplementary material for an analogous figure of the Landsat data.  
 362

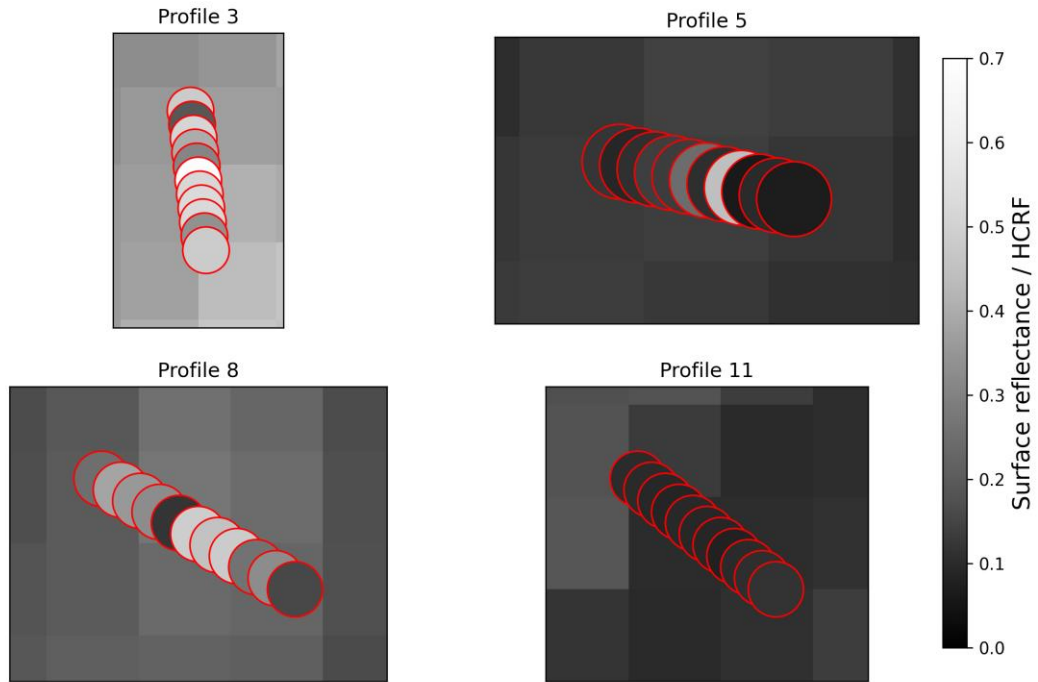
363 Table 3: Band names and respective wavelength range and resolution for Landsat and Sentinel as used in this study.  
 364 Pearson correlation given for mean band values of ground-measurements and associated satellite data. For Landsat, the  
 365 solar zenith and azimuth angles given in the surface reflectance image are listed. The view zenith angle is hardcoded to  
 366 0 in the Land Surface Reflectance Code (LaSRC\_1.3.0) for the Landsat surface reflectance product, as per the LaSRC  
 367 documentation (USGS, 2020). For Sentinel, the incidence angles refer to the mean viewing zenith and azimuth angles  
 368 for each band. The solar angles are the averages for all bands.  
 369

Band	Range (nm)	Resolution (m)	Pearson Corr.	View zenith angle	View azimuth angle	Solar zenith angle	Solar azimuth angle
	<b>Landsat</b>	Sensing time: 2019-09-03 10:10 GMT					

1 (Coastal/Aerosol)	430-450	30	0.62	0	-	42.63	153.57
2 (Blue)	450-510	30	0.61				
3 (Green)	530-590	30	0.58				
4 (Red)	640-670	30	0.57				
5 (NIR)	850-880	30	0.53				
	<b>Sentinel</b>	Sensing time:2019-09-04 10:20 GMT		<b>Mean incidence zenith angle</b>	<b>Mean incidence azimuth angle</b>	<b>Mean solar zenith angle</b>	<b>Mean solar azimuth angle</b>
1 (Coastal/Aerosol)	433-453	60	0.46	3.13	193.02	40.83	159.93
2 (Blue)	457.5-522.5	10	0.65	2.48	198.51		
3 (Green)	542.5-577.5	10	0.63	2.59	196.22		
4 (Red)	650-680	10	0.61	2.72	194.92		
5 (Vegetation Red Edge)	697.5-712.5	20	0.57	2.79	194.43		
6 (Vegetation Red Edge)	732.5-747.5	20	0.56	2.87	193.84		
7 (Vegetation Red Edge)	773-793	20	0.55	2.95	193.53		
8 (NIR)	784.5-899.5	10	0.56	2.54	197.22		
8A (NIR narrow band)	855-875	20	0.53	3.04	193.30		
9 (Water vapour)	953-955	60	0.3	3.22	192.89		

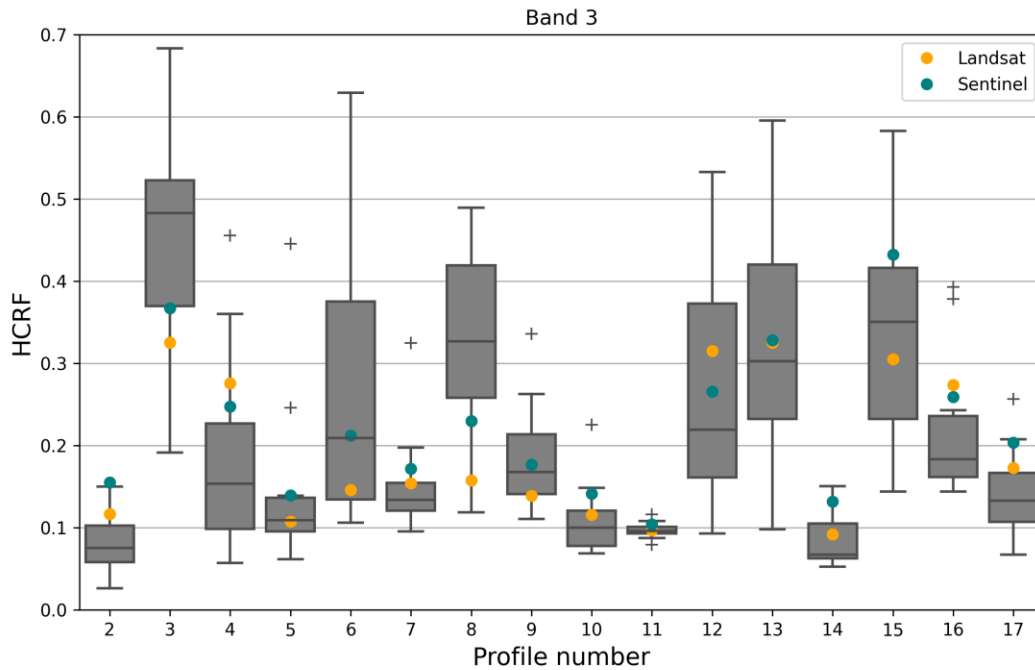
370  
371  
372  
373  
374

Sentinel - band 3



375  
376 Figure 67: The spectra comprising the profile lines are plotted over the corresponding satellite pixels for selected  
377 profiles. The colour bar is the same for the background raster and the circles indicating the sampling sites of the spectra  
378 and represents the Sentinel band 3 pixel value and the mean reflectance in the Sentinel band 3 wavelength range of each  
379 spectrum, respectively. The pixel size of the raster is 10m<sup>2</sup>. The GPS coordinates of the sampling sites are centred in the  
380 circles. The circle radius is set to 3m to represent the horizontal uncertainty of the GPS points.  
381

382 The spread of in situ HCRF values per profile is generally lower for profiles that are darker overall, and greater for  
383 brighter profiles, although not in all cases (Fig. 3, Fig. 78). In the Sentinel band 3 wavelength range, profile 3 is  
384 brightest with a median reflectance of 0.48 and spread of 0.49. Profile 6 (median in Sentinel band 3 range: 0.21) has the  
385 largest spread of HCRF (0.52). Broadly speaking, profiles with a high median HCRF tend to include individual  
386 measurement points that are both very bright and very dark, while darker profiles are more uniformly dark. Profile 6 in  
387 particular transitions between surface types and contains wet/dirty spectra as well as dry ice spectra (see Table 2).  
388 Figure 78 shows boxplots of the ground measurements (band 3 mean) for all profiles to exemplify this and indicates  
389 where the Landsat and Sentinel values fall compared to the spread of values in each profile.



390

391

392 Figure 78: Spread of the Sentinel band 3 (wavelength range: 542.5-577.5 nm) mean values of the measured spectra,  
 393 grouped by profile. Orange and blue circles show corresponding mean pixel values of data extracted from Landsat and  
 394 Sentinel pixels at the sampling sites of the spectra, respectively. The boxes represent the first and third quartile. The  
 395 whiskers represent 1.5x the interquartile range, the + symbols are outliers.

396

397 When binning in situ measurements by the associated satellite value/pixel and taking the median or mean of the binned  
 398 values, the difference between the median/mean in situ value and the satellite value tends to decrease with increasing  
 399 number of in situ measurements mapped to unique satellite values. This is to be expected, as each satellite value  
 400 represents an integration of the emission characteristics over the area contained in the pixel. However, for our data, this  
 401 relationship is not obviously linear and differs between Sentinel and Landsat, as well as between different bands (Figure  
 402 89).

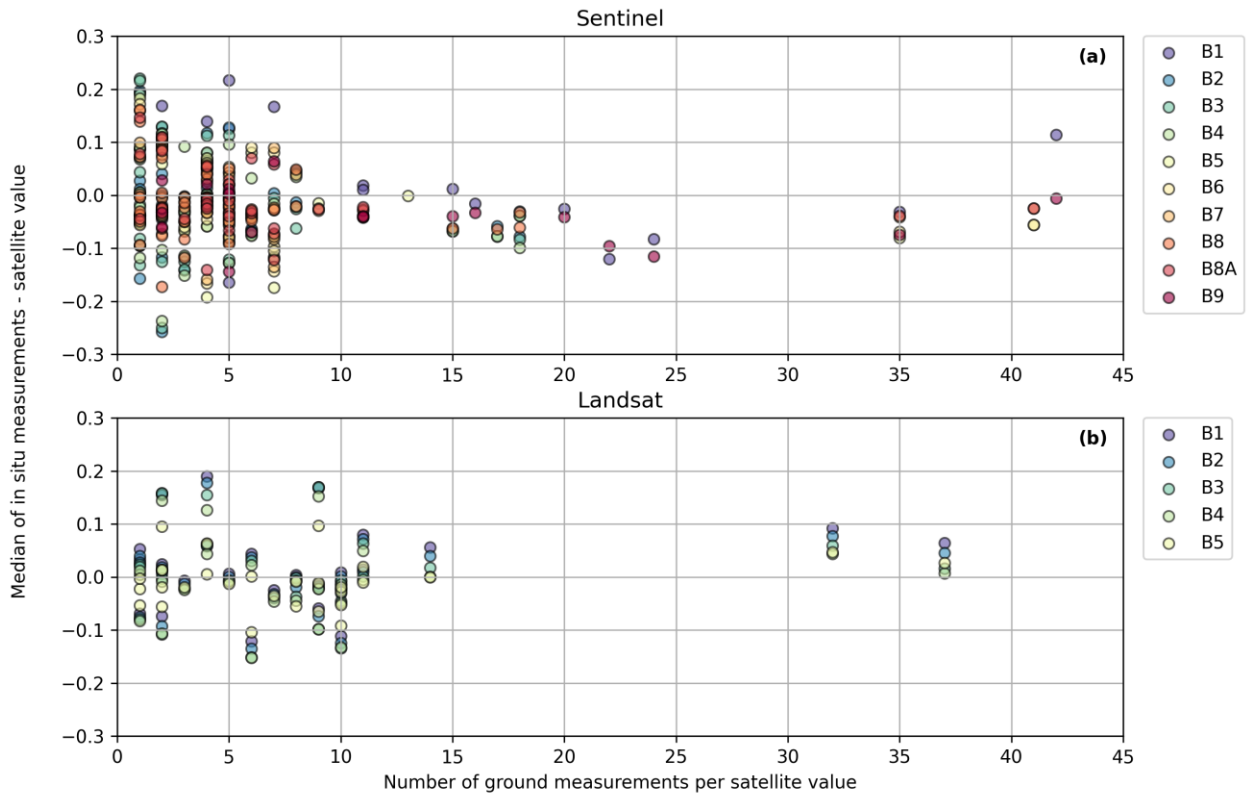
403

404 Comparing in situ and satellite values for individual in situ measurement points, it is apparent that both satellites tend to  
 405 overestimate the reflectance values of dark ground surfaces, and underestimate the reflectance of bright surfaces, in all  
 406 bands (Figure 94). The shift from over- to underestimation appears linear and has a similar increase rate in all bands.  
 407 The zero crossings of the regression lines, i.e. the ground reflectance values for which ground measurements and  
 408 satellite values match, fall between 0.15 (band 5) and 0.21 (band 1) for Landsat and 0.17 (band 9) and 0.27 (band 3) for  
 409 Sentinel.

410

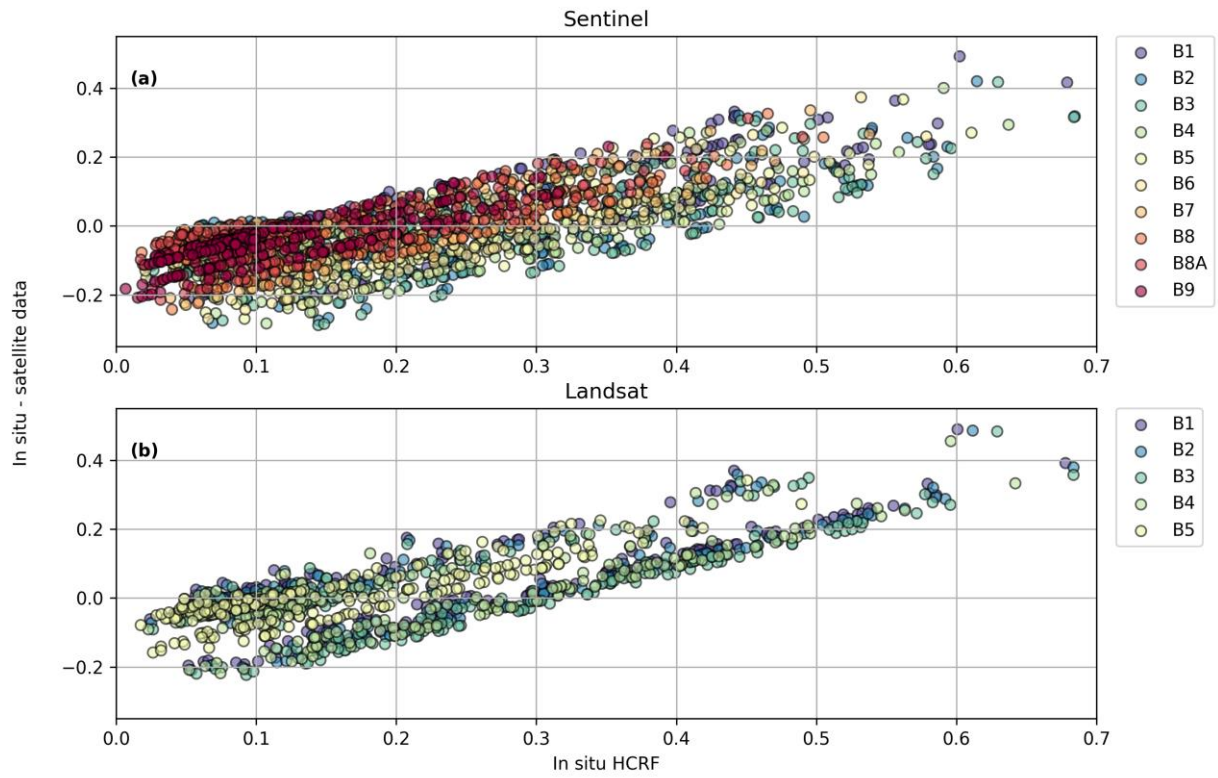
411 Figure 104 shows histograms of the mean reflectance in band 3 of Landsat and Sentinel, respectively, compared with  
 412 associated in situ values, as well as density plots of the satellite derived surface reflectance over all pixels in the study  
 413 area. The mean is highest in the in situ measurements and lowest in Landsat images. Both Sentinel and Landsat fail to  
 414 capture HCRF values below 0.05 and above 0.45. A second peak in frequency evident from the in situ measurements at  
 415 a reflectance of 0.4 is not represented in the remote sensing data.

416

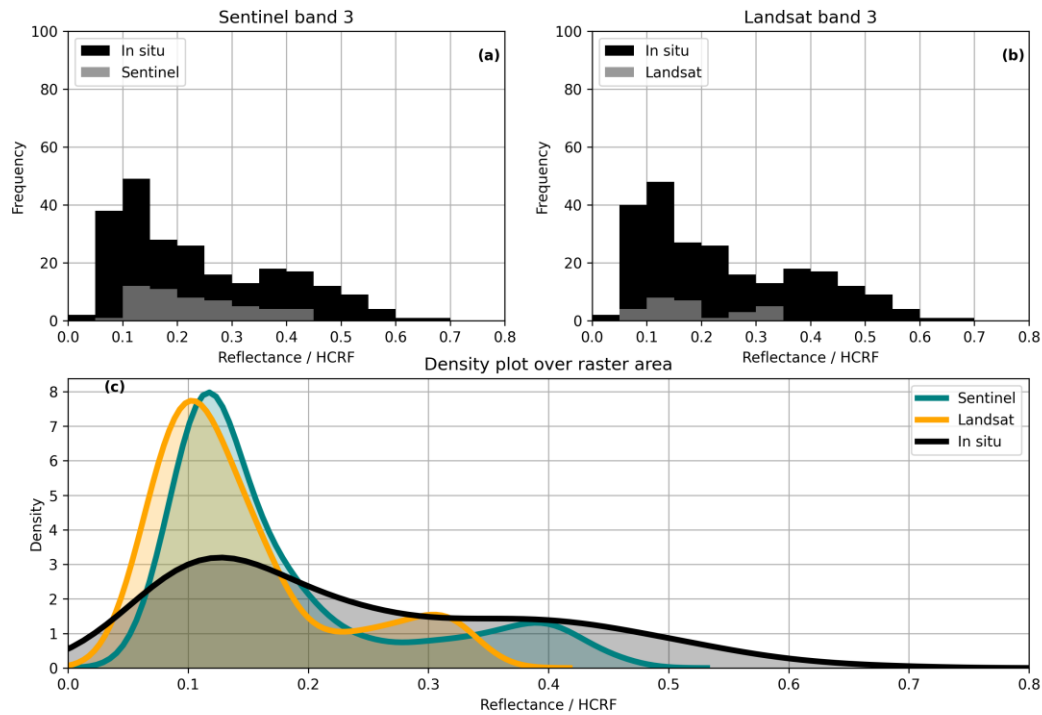


417  
 418  
 419 Figure 89: The number of ground measurements per unique satellite value (x-axis) is plotted against the difference  
 420 between the median of these ground measurements in the respective wavelength band and the corresponding satellite  
 421 value (y-axis). i.e. values that are positive in the vertical axis represent cases where ground reflectance is higher than  
 422 satellite derived reflectance, whereas negative values represent the opposite. Different colours represent the different  
 423 satellite bands, as indicated by the legend next to the plots.  
 424





425  
 426  
 427 Figure 940: Same data as in Fig. 840, but showing individual sampling points without grouping by common satellite  
 428 pixels.  
 429  
 430  
 431



432  
433  
434  
435  
436  
437  
438  
439

Figure 104: The histograms in the top panels (a, b) show the frequency of occurrence of the band 3 mean values of the ground measurements per reflectance bin. Bin width: 0.05. Overlaid in grey are the histograms of the corresponding satellite pixel values. The bottom panel (c) shows density plots of the Sentinel and Landsat band 3 surface reflectance rasters over the study area (smallest possible rectangle containing all ground measurements), with the density of the in situ HCRF for comparison.

440  
441  
442  
443  
444  
445  
446  
447  
448  
449  
450  
451  
452

To conclude the results, a note on the sensitivity of data and results to the spatial resolution of the satellite data and the accuracy of the geolocation of the in situ data: To assess the possible effects of the GPS accuracy or lack thereof, we compare the differences between in situ and satellite values presented previously to the differences that result when a buffer corresponding to the GPS uncertainty is created around each in situ measurement point. For the Sentinel data in the original 10 m resolution of band 3, the maximum number of pixels that any buffer touches is 4, the mean is 2.6, and most buffered in situ measurement points overlap with 2 pixels. For the 30 m Landsat data in band 3, the maximum number of pixels touched is also 4 while the mean is 1.5 and most in situ points are fully within only one pixel. Table 4 gives the standard deviation of differences between the in situ HCRF and the satellite data in different resolutions, grouped by the number pixels the buffered measurement points overlap with, to show how variability of results shifts depending on the buffer and the raster resolution. Changes caused by introducing the buffer are small in all groups. As expected, standard deviation increases with decreasing resolution of the satellite pixels due to the loss of detail in the satellite data. Figure 112 gives an overview of the ungrouped dataset with and without the buffer and at different raster resolutions.

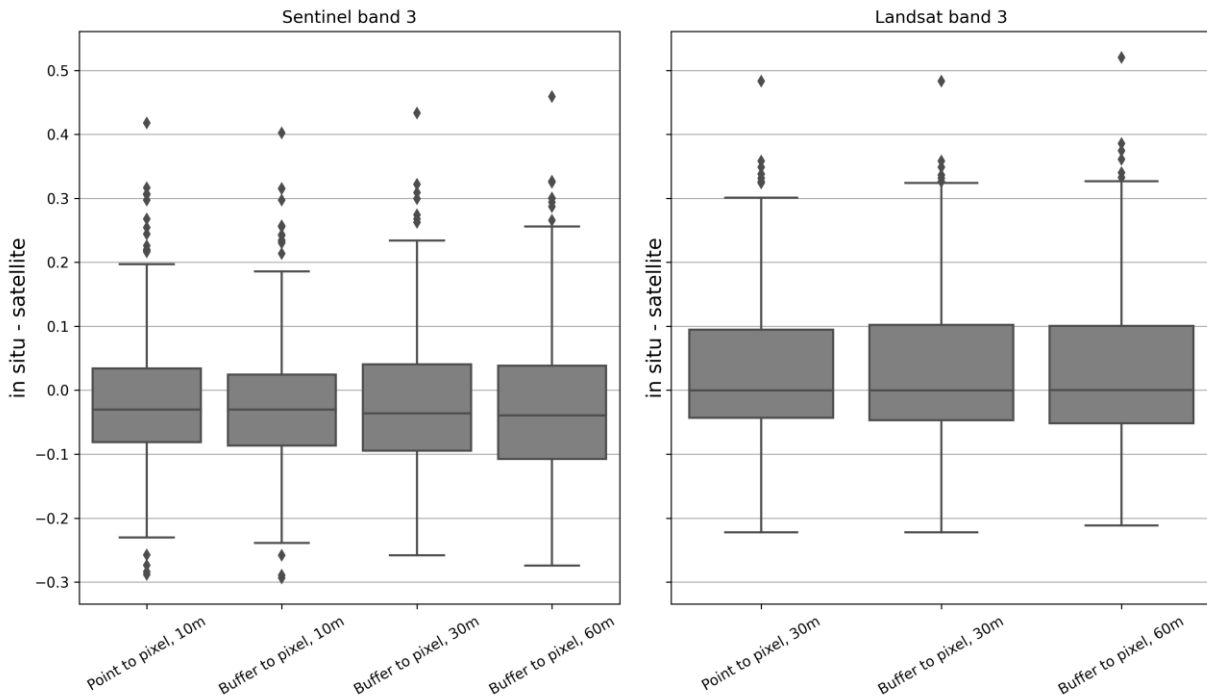
453  
454  
455

Table 4: Comparison of in situ and satellite data by the standard deviation (SD) of the difference between in situ HCRF and satellite surface reflectance. Values are grouped by number of pixels that buffered in situ measurements overlap.

	Sentinel					Landsat			
Nr. of overlapping pixels	Nr. of points	SD, no buffer, 10m	SD, buffer, 10m	SD, buffer, 30m	SD, buffer, 60m	Nr. of points	SD, no buffer, 30m	SD, buffer, 30m	SD, buffer, 60m
1	25	0.098	0.098	0.108	0.129	134	0.129	0.129	0.134
2	124	0.119	0.118	0.120	0.124	94	0.106	0.107	0.103

3	9	0.057	0.065	0.069	0.099	1	-	-	-
4	76	0.122	0.121	0.127	0.136	5	0.082	0.074	0.083

456



457

458

459

460

461

462

463

464

Figure 112: For the respective Sentinel and Landsat band 3 wavelength range, the difference between the in situ HCRF and satellite surface reflectance product is on the vertical axis. Point to pixel refers to the data as presented in previous figures. Buffer to pixel refers to data generated using a buffer around the in situ measurement points to account for GPS accuracy. For Sentinel, the original 10m resolution data was resampled to 30 and 60m. For Landsat, the original 30m resolution data was resampled to 60m.

#### 4. Discussion

465

466

467

468

There are a number of complexities associated both with measuring reflectance properties on the ground and with any comparison between different products and data sets. Perhaps more than anything else, our results highlight the need for further in situ measurements and targeted data collection campaigns designed specifically to address some of the uncertainties detailed in the following.

469

470

##### 4.1. Reflectance anisotropy and changing solar and atmospheric conditions

471

472

473

474

475

476

477

478

479

480

481

482

483

484

485

Ice is an anisotropic material and previous studies have shown that for glacier surfaces, anisotropy increases with decreasing albedo and depends on wavelength and solar zenith angle (Greuell and de Wildt, 1999; Klok et al., 2003; Naegeli et al., 2015). In order to truly quantify the effects of anisotropy in in situ spectroradiometric measurements, the bidirectional reflectance distribution function (BRDF) must be obtained – ideally for each measurement point. The BRDF cannot be measured directly but is approximated, e.g. by interpolating between multi-angular spectroradiometer measurements (Naegeli et al., 2015), or with modelling approaches (Malinka et al., 2016). While multi-angular HCRF measurements allow for the estimation of the BRDF, they are intrinsically dependent on the atmospheric conditions (cloud cover) at any given time, as well as on the topography and structure of the surface. Naegeli et al. (2015, 2017) use this approach to develop anisotropy correction factors for different glacier surface types in order to account for the typical underestimation of albedo in observations from nadir in remote sensing data. They find a difference between corrected and uncorrected albedo values of up to 11% for dirty ice in airborne imaging spectroscopy data. Nonetheless, the application of constant correction factors for clustered surface types is a simplification that obscures both the gradational nature of surface classification and the complexity of accounting for the effects of varying surface roughness on effective illumination angles. We consider a quantitative assessment of anisotropy beyond the scope of our study and hope to tackle this issue in detail in future work. We assume that our in situ data as well as the satellite

486 products underestimate the quantities they measure (HCRF and surface reflectance as per the respective documentation  
487 of the satellite products) due to the nadir or near-nadir observational angle, in particular for dark surfaces, and that  
488 uncertainties caused by anisotropy are likely to be in the range found by Naegeli et al. (2017). The local variability of  
489 reflectance properties of glacier ice is comprised of the spectral, as well as spatial and temporal variability of reflectance  
490 anisotropy, which require a combination of targeted, continuous measurements and modelling that accounts for the  
491 surface roughness of different glacier surface types to truly delineate.

492 The weather on September 3 (Landsat overpass) and September 4, 2019, (Sentinel overpass, in situ measurements) was  
493 very favourable. There was no cloud cover at the study site during either of the satellite overpasses and for the duration  
494 of the field measurements and we consider any changes in atmospheric conditions to be negligible. While the  
495 illumination angles naturally change over the course of the day and accordingly changed during the in situ  
496 measurements (Table 2), very low solar elevation angles were avoided. In their study on parametrizing BRDFs for  
497 glacier ice and Landsat TM, Greuell and de Wildt (1999) show that the spectrally integrated albedo of dark ice changes  
498 with the solar zenith angle and is particularly low for low zenith angles. Accordingly, we acknowledge that the changing  
499 solar angles are a source of uncertainty in our data and the comparison with the satellite derived reflectances, but we  
500 consider this uncertainty relatively small since measurements were carried out within a few hours before and after the  
501 satellite overpasses, avoiding very low solar elevation angles. Greuell and de Wildt (1999) also point out that the drop in  
502 albedo for low zenith angle is related to the presence of meltwater at later times of day (lower zenith angles), which  
503 highlights the difficulty of isolating one variable (zenith angle) in a complex system with multiple variables that change  
504 over time (surface processes like meltwater affecting reflectance properties).

505 The Landsat and Sentinel surface reflectance products both incorporate an atmospheric correction applied to TOA  
506 reflectance in the generation of the BOA product (Vermote et al., 2016; Main-Knorn et al., 2017). This introduces some  
507 uncertainty into the comparison with in situ data since the correction methods differ. Nonetheless, we believe that  
508 assessing how in situ data compare to the frequently used surface reflectance products of the Landsat-8 and Sentinel-2  
509 suites is a necessary first step in being able to determine whether custom atmospheric corrections would improve results  
510 and if such improvements would be large enough to outweigh the added complexity and computational cost. We suggest  
511 that the answer to this question depends on the application and the spatial scale of the intended analysis. Again, this is  
512 beyond the scope of the presented study and is a point that needs to be specifically addressed in future work. We suggest  
513 that case studies at individual, well-studied glaciers can serve as an ideal testing ground for such issues, and will help to  
514 determine whether custom atmospheric corrections should be applied and are feasible on a regional or even global scale  
515 in satellite-based studies of ablation area reflectance properties.

#### 516 **4.2. Implications of in situ and satellite comparison**

517 The results presented in section 3.1. highlight the large spatial variability of HCRF and different surface types  
518 encountered in the ablation area, both of which are in line with findings from other studies (Naegeli et al., 2015, 2017;  
519 Di Mauro et al., 2017). Section 3.2., the comparison of the in situ data with satellite values, arguably presents greater  
520 challenges in terms of interpretation and implications of the results.

521 In summary, there are three key findings which we believe may be important for further studies and for delineating the  
522 relationship between in situ and satellite derived reflectance:

- 523 • Sentinel surface reflectance values tend to be closer to the higher end of HCRF values measured in situ, while  
524 Landsat tends to be closer to the in situ minimum.
- 525 • The difference between in situ data and satellite data tends to decrease when there are more in situ data points  
526 per pixel, but not always and not in a clearly linear way.
- 527 • The reflectance of dark surfaces tends to be overestimated in the satellite products, while the reflectance of  
528 bright surfaces tends to be underestimated.

529 Explaining the above points in full requires targeted investigations specifically addressing the contributing factors and  
530 uncertainties, which – with our current data set – we can only provide a qualitative overview of:

531 As mentioned previously, different atmospheric corrections are used for the Sentinel and Landsat surface reflectance  
532 products. This may contribute to systematic differences in how surface reflectance is represented under differing  
533 lighting conditions and in different spectral ranges. Efforts to harmonize the Landsat and Sentinel surface reflectance  
534 data sets have great potential for minimizing this problem for applications where data from both satellites is used  
535 (Claverie et al., 2018).

536 Another issue that deserves more detailed attention is the narrow/spectral to broad band conversion required for  
537 comparing satellite reflectance in individual bands with the in situ data of the same wavelength range. We intentionally  
538 do not compute a shortwave broadband albedo from the satellite band values or the spectral in situ data to avoid  
539 introducing a further source of uncertainty. Instead, we limit ourselves to averaging over the band wavelength range in  
540 order to keep the comparison as straightforward as possible, but acknowledge that a glacier wide broad band albedo is a  
541 key parameter for many regional or global modelling applications.

542 The standard atmospherically corrected BOA reflectance products from satellite data are provided without correcting  
543 for the BRDF. The BRDF, describing the change of the reflectance with different observation and incidence geometries,  
544 can have a significant impact on the satellite-based reflectance as well as on the in situ data, leading to inherent  
545 challenges when comparing satellite based BOA reflectance with in situ reflectance measurements (Schaeppman-Strub et  
546 al., 2006). Correcting Landsat and Sentinel surface reflectance with MODIS or VIIRS BRDF products to produce  
547 surface albedo has been shown to be a viable approach in some cases (Shuai et al., 2011; Li et al., 2018), but the coarse  
548 resolution of MODIS and VIIRS data is unlikely to capture the small-scale anisotropy effects of different glacier surface  
549 types. This would therefore be of limited use for our purposes. Optimizing methods for computing surface albedo from  
550 the L2A products, as well as from the in situ HCRF, requires further study and customized solutions accounting for  
551 local topographic effects and the spectral characteristics of the surfaces. We assume that for our case uncertainties due  
552 to the intrinsic difference between HCRF and satellite derived HDRF are small compared to other sources of  
553 uncertainty: The influence of local topography as a source of indirect radiation is not represented in the satellite derived  
554 values and the microstructure of the ice surface may locally affect in situ values on a scale that not visible to the  
555 satellite, but could be very significant for in situ measurements (e.g. small ice ridges or similar features acting as  
556 reflectors and/or scattering light into the FOV of the instrument).

557 Hendricks et al. (2004) state for spectroradiometric measurements at Hintereisferner compared to Landsat ETM+  
558 imagery acquired about 2 weeks before the field measurements: “The reflectance of ice seems to be highly variable with  
559 both under- and overestimations of up to 76 % and 31 % respectively.” This corresponds well with our finding that both  
560 under- and overestimation occur frequently for both satellites. The factors mentioned above may partly explain the  
561 location of the shift from under- to overestimation (Fig. 9), but –again– targeted measurement campaigns are needed to  
562 truly quantify this.

563 The influence of very local backscattering could play a role in the seeming inconsistencies in the dependency of the  
564 difference between in situ and satellite data on the number of in situ measurement points per pixel (Fig. 810), but this  
565 also ties in with questions regarding the positional accuracy of the in situ measurement points and the satellite data, and  
566 the spatial representativity of point measurements for a larger area:

567 Our comparison of in situ and satellite data is based on the assumption that we know where both are located in a  
568 common coordinate reference system to a sufficient degree of accuracy. The accuracy of the position of the GPS points  
569 at the start and end points of the measurement profiles is approximately 3m. Sentinel-2 orthorectification is based on the  
570 PlanetDEM 90 digital elevation model (DEM), which incorporates the SRTM DEM in areas where SRTM is available,  
571 such as Austria (Kääb et al. 2016). The geometric accuracy of the Sentinel data hence depends on the accuracy of the  
572 underlying DEM, which is subject to a number of uncertainties particularly over mountainous terrain. Vertical  
573 inaccuracies – which propagate into horizontal inaccuracies - increase over glacier surfaces, especially in areas with  
574 large changes in surface elevation, as the DEM can only provide a snapshot of conditions for a moment in time and  
575 quickly becomes outdated in rapidly changing environments. Pandžić et al (2016) determine an average offset in the  
576 Sentinel-2 data for Austria of about 6m compared to a high-resolution regional DEM. The performance requirement of  
577 Landsat-8 OLI for geometric terrain corrected accuracy is specified as 12m (Storey et al, 2014). Kääb et al. (2016) find  
578 cross-track offsets of 20-30 m over glacier termini in the Swiss Alps when comparing Landsat-8 and Sentinel-2 scenes  
579 acquired on September 8, 2015. Accordingly, uncertainties regarding the GPS points of the in situ measurements as  
580 delineated in our sensitivity analysis (Table 4, Figure 112) can be considered relatively small compared to the those  
581 related to the orthorectification of the satellite data. Comparisons between in situ point data and pixel values from the  
582 satellite products must be interpreted keeping positional uncertainties in mind.

583 Decreasing the pixel resolution and averaging over multiple in situ measurement points can serve as an approach to  
584 reduce the influence of geometric errors. However, any sort of averaging procedure must also be assessed in terms of  
585 spatial representativeness of the point measurements for a greater area and, conversely, the down sampled satellite data  
586 for small scale surface processes. What can be considered representative will always be a question of scale and  
587 application. The glacier surface at the study site is locally very heterogenous and hence prone to representativeness  
588 errors (Wu et al., 2019). We selected the location of the in situ profile lines so that they cover what we consider to be the

589 typical surface features and types of a given section of the ablation zone and argue that our 20 m long profile lines with  
590 equidistant measurements at least every two meters capture any variations that are likely to influence the corresponding  
591 pixel values of the satellite data. Naturally, the less overlap there is between the profile lines and any given satellite  
592 pixel, the more likely it is that the in situ point data happen to capture something that differs strongly from what the  
593 satellite sees.

594 The different surface types identified at Jamtalferner (Fig. 45) and their reflectance spectra are comparable to types of  
595 surfaces identified in Switzerland at Morteratsch and Glacier de la Plaine Morte by Di Mauro et al. (2017) and Naegeli  
596 et al. (2015), respectively, supporting the use of a classification scheme based on differentiating between a) clean and  
597 dirty ice surfaces and b) the presence or absence of liquid water on the ice surface. Classifying the surface  
598 characteristics into discrete types can help to ensure representativeness e.g. by quantifying how much of a given area  
599 subsection relevant to the comparison with remote sensing data is comprised of which type and then sampling  
600 accordingly. However, surface types are not always discrete in practice. Nicholson and Benn (2006) indicate that the  
601 surface albedo of ice with scattered debris can be simulated in a modelling approach be linearly varying between clean  
602 ice albedo values and values for debris, but this does not necessarily account for other types of surfaces and even the  
603 clean ice albedo can vary considerably, especially if liquid water is present. Additionally, classification by type of any  
604 kind cannot address the issue of temporal representativeness unless the temporal variability of different surface types is  
605 first determined.

606 Profile 8 shows particularly poor agreement with the corresponding satellite data and may be an example where  
607 temporal variability plays a role: The profile crosses a section of ice where the contrast between dark and bright areas is  
608 comparatively strong. The profile line is roughly at a right angle to the flow direction of the glacier and “stripes” of  
609 meltwater channels and/or dirt cross the line. The profile has a comparable number of individual spectra with  
610 reflectance values above and below the profile mean, i.e. it is not a dark profile with a few bright outliers (compare e.g.  
611 to P6 in Fig. 67) or vice versa (e.g. P3), but alternates along the profile line. Agreement with the remote sensing data is  
612 decent for the darker spectra in P8 but the bright values are not captured. While we cannot rule out that the lack of  
613 agreement between the field and remote sensing data is due to an unusually unfortunate/unrepresentative positioning of  
614 the field measurement points in the satellite pixels, this may be an instance where the diurnal melt cycle and the  
615 associated presence/absence of water on the surface exacerbates the contrast between the dark and bright sections of the  
616 profile. In the bright sections, the porous weathering crust and cryconite hole structures appear to be drained of water,  
617 while the depressions of the melt channels are noticeably wet. Cook et al. (2016) indicate the occurrence of “sudden  
618 drainage events” in the weathering crust on a day-to-day time scale and a diurnal cycle of the hydrology of the  
619 weathering crust driven by meteorological conditions (radiation, turbulent fluxes). The time of day of a satellite  
620 overpass would determine which stage of this cycle the satellite sees and consequently the satellite data would not  
621 capture this variability. In order to assess how much the time of day of the overpass could systematically affect the  
622 representativeness of the satellite data for actual ground reflectance, it needs to be determined how significant and how  
623 consistent the diurnal cycle is. To do this, the driving processes must be identified, keeping in mind that these may be  
624 different for different types of glaciers and that different causes of short-term albedo change can overlap. E.g.: Azzoni et  
625 al. (2016) point out that meltwater increases albedo around midday in a daily cycle, while rain causes increased albedo  
626 for up to 4 days after the precipitation event. A seasonal cycle of albedo has been demonstrated in previous  
627 observational studies and modelling efforts of broadband albedo, highlighting the importance of continuous  
628 measurements (e.g. Hoinkes and Wendler, 1968; Nicholson and Benn, 2012; Möller and Möller, 2017).

### 629 4.3. Relevance of small-scale variability

630 The reflectance properties of ice are a central part of mass and energy balance modelling, usually in the form of a  
631 glacier wide broadband albedo, or using one value for ice in the ablation zone and one for snow covered areas.  
632 Resolving local albedo variations at a very small, sub-pixel scale is not required for regional or global studies, provided  
633 the albedo parametrization captures the conditions on the ground adequately for the region of interest. In their important  
634 2015 study, Naegeli et al. find that Sentinel-2 and Landsat-8 reflectance data are within the suggested accuracy  
635 requirements for global climate modelling ( $\pm 0.05$ , Henderson-Sellers and Wilson, 1983) over their study site, Glacier de  
636 la Plaine Morte in Switzerland. In the same study, they report a 10% difference in modelled mass balance when a  
637 spatially distributed albedo is used to force the model as opposed to a single, glacier wide albedo. Significantly larger  
638 differences occur in parts of the glacier where water is present on the surface or the ice surface contains a lot of light-  
639 absorbing impurities. While the glacier-wide impact of a spatially distributed albedo on model results may be relatively  
640 small, this highlights that resolving local variability of reflectance properties and its causes is important for accurately  
641 predicting the future evolution of individual glaciers, especially in cases where the firn covered area is gone or greatly

642 reduced and rapid melt is occurring. Only once the problem of different scales comparing point and spatially averaged  
643 data is solved, the relationship between albedo variability and mass balance point and averaged data can be tackled to  
644 calculate the effects on mass balance at glacier-wide or regional scale.

645 Aside from directly mass and energy balance related applications, reflectance data with high spatial and temporal  
646 resolution is essential to improve understanding of micro-hydrological processes in the weathering crust and how these  
647 may affect a possible larger scale darkening of increasingly snow free glaciers, e.g. by favoring or impeding the growth  
648 of ice algae, or the collection/washing out of cryoconite or other impurities. High resolution time series of spectral  
649 reflectance at representative locations in the ablation zone are needed to assess how changes in wetness and  
650 temperature, surface texture (cryoconite formation, roughness changes during the season), biotic productivity,  
651 deposition of sediment by melt water and rain affect reflectance properties on a small spatial scale, throughout the day  
652 and over the course of the ablation season. Establishing measurement efforts aimed at generating such time series on  
653 glaciers with existing mass balance monitoring networks would be highly desirable in order to better link small scale  
654 surface processes with mass and energy balance modelling.

## 655 656 **5. Conclusion & Outlook**

657  
658 In comparing our in situ measurements with readily available L2A satellite products, we chose an “as simple as  
659 possible” approach to gain a general understanding of where sources of uncertainties are. We found that the difference  
660 between in situ and satellite data is not uniform across satellite bands, between Landsat and Sentinel, and to some extent  
661 between surface types. Reflectance variability on the ground is not fully represented in the satellite data, which raises  
662 questions as to how well surface processes at rapidly changing glaciers such as Jamtalferner can be resolved with  
663 satellite data.

664 The reflectance properties of ice, along with other feedback mechanisms such as changing topography and glacier  
665 geometry, significantly impact the rate of glacial retreat, contributing to the non-linear characteristics of glacier change  
666 and the high variability of defining parameters such as mass-balance or area change even among neighbouring glaciers  
667 subject to common climatic drivers (Charalampidis et al., 2018). Understanding these feedback mechanisms and  
668 associated processes is key to successfully predicting future glacier changes across spatial and temporal scales. Ice  
669 albedo will remain a significant source of uncertainty in modelling applications as long as the processes governing  
670 temporal and spatial variability are not fully understood.

671 Quantifying spatial and temporal variability of spectral reflectance and delineating the main causes of this variability for  
672 individual glaciers will improve modelling capabilities of glacier evolution and catchment hydrology. Satellite-derived  
673 reflectance products are a key component of tackling similar questions on the regional and global level. However,  
674 ground truth data from representative sites is essential in order to understand uncertainties associated with satellite  
675 albedo and surface reflectance products and potentially improve them for specific contexts.

676 Moving forward, an expansion of the monitoring network at Jamtalferner and, ideally, other glaciers, by continuous  
677 reflectance measurements in the ablation zone at a fixed location is needed, as well as “snap-shot” measurements of  
678 spectral, multi-angular reflectance at multiple strategic points in regular intervals. Combining analysis of spectral  
679 reflectance data from in situ and remote sensing sources with the wealth of contextual information available at  
680 Jamtalferner and other established monitoring sites has the potential to greatly improve our understanding of the  
681 complex interplay of surface changes, glacier dynamics, and mass- and energy balance.

## 682 683 684 **Author Contribution**

685  
686 L. Felbauer and A. Fischer collected the in situ data. Subsequent data curation was carried out by L. Felbauer and L.  
687 Hartl. G. Schwaizer conceptualized the comparison of in situ and satellite derived data. L. Hartl developed the code for  
688 data analysis and visualizations, and wrote the manuscript with contributions from all co-authors.

## 689 690 **Competing interests**

691  
692 The authors have no competing interests to declare.

## 693 694 **Data availability**

695  
696 The spectral reflectance data can be downloaded at: <https://doi.pangaea.de/10.1594/PANGAEA.915932>  
697 And interactively explored in a web-app at: <http://spectralalbedo.mountainresearch.at/>  
698

## 699 **Acknowledgements**

700  
701 We are very grateful to Gottlieb Lorenz and the entire team at the Jamtal Hütte for providing an excellent base for field  
702 work at Jamtalferner and invaluable support over the years. We sincerely thank M. Pelto and the second, anonymous  
703 reviewer for their helpful comments!  
704

## 705 **References**

706  
707 Alexander, P. M., Tedesco, M., Fettweis, X., Van De Wal, R., Smeets, C. J. P. P., and Van Den Broeke, M. R.: Assessing  
708 spatio-temporal variability and trends in modelled and measured Greenland Ice Sheet albedo (2000-2013), *The*  
709 *Cryosphere*, 8(6), 2293-2312, 2014.

710 ASD Inc.: FieldSpec® HandHeld2™ Spectroradiometer User Manual.  
711 [https://www.malvernpanalytical.com/en/support/product-support/asd-range/fieldspec-range/handheld-2-hand-held-vnir-](https://www.malvernpanalytical.com/en/support/product-support/asd-range/fieldspec-range/handheld-2-hand-held-vnir-spectroradiometer#manuals)  
712 [spectroradiometer#manuals](https://www.malvernpanalytical.com/en/support/product-support/asd-range/fieldspec-range/handheld-2-hand-held-vnir-spectroradiometer#manuals), Accessed: Sep. 22, 2020.

713 Azzoni, R. S., Senese, A., Zerboni, A., Maugeri, M., Smiraglia, C., and Diolaiuti, G. A.: Estimating ice albedo from fine  
714 debris cover quantified by a semi-automatic method: the case study of Forni Glacier, Italian Alps, *The Cryosphere*, 10,  
715 665-679, 2016.

716  
717 Box, J. E., Fettweis, X., Stroeve, J. C., Tedesco, M., Hall, D. K., and Steffen, K.: Greenland ice sheet albedo feedback:  
718 thermodynamics and atmospheric drivers, *The Cryosphere*, 6(4), 821-839, 2012.

719 Box J. E., van As D., and Steffen, K. Greenland, Canadian and Icelandic land-ice albedo grids (2000–2016). *Geological*  
720 *Survey of Denmark and Greenland Bulletin*, 38, 53-56, 2017.

721 Brun, F., Dumont, M., Wagnon, P., Berthier, E., Azam, M. F., Shea, J. M., Sirguey, P., Rabatel, A., and Ramanathan, A.:  
722 Seasonal changes in surface albedo of Himalayan glaciers from MODIS data and links with the annual mass balance,  
723 *The Cryosphere*, 9(1), 341-355, 2015.

724  
725 Charalampidis, C., Fischer, A., Kuhn, M., Lambrecht, A., Mayer, C., Thomaidis, K., and Weber, M.: Mass-budget  
726 anomalies and geometry signals of three Austrian glaciers, *Frontiers in Earth Science*, 6, p. 218, 2018.

727  
728 Claverie, M., Ju, J., Masek, J.G., Dungan, J.L., Vermote, E.F., Roger, J.C., Skakun, S.V. and Justice, C.: The  
729 Harmonized Landsat and Sentinel-2 surface reflectance data set. *Remote sensing of environment*, 219, pp.145-161,  
730 2018.

731 Cook, J.M., Hodson, A.J. and Irvine-Fynn, T.D.: Supraglacial weathering crust dynamics inferred from cryoconite hole  
732 hydrology. *Hydrological Processes*, 30(3), pp.433-446, 2016.

733 Dirmhirn, I. and Trojer, E.: Albedountersuchungen auf dem Hintereisferner, *Archiv für Meteorologie, Geophysik und*  
734 *Bioklimatologie, Serie B*, 6(4), pp.400-416, 1955.

735  
736 Dumont, M., Brun, E., Picard, G., Michou, M., Libois, Q., Petit, J. R., Geyer, S., and Josse, B.: Contribution of light-  
737 absorbing impurities in snow to Greenland's darkening since 2009, *Nature Geoscience*, 7(7), 509, 2014.

738  
739 Fischer, A.: Comparison of direct and geodetic mass balances on a multi-annual time scale. *The Cryosphere*, 5, pp.107-  
740 124, 2011.

741  
742 Fischer, A., Helfricht, K., Wiesenegger, H., Hartl, L., Seiser, B., and Stocker-Waldhuber, M.: Chapter 9 - What Future  
743 for Mountain Glaciers? Insights and Implications From Long-Term Monitoring in the Austrian Alps, in: *Developments*  
744 *in Earth Surface Processes*, edited by: Greenwood, G., B. and Shroder, J. F., Elsevier, 21, 325-382, 2016.

745  
746 Fischer, A., Markl, G., and Kuhn, M.: Glacier mass balances and elevation zones of Jamtalferner, Silvretta, Austria,  
747 1988/1989 to 2016/2017, Institut für Interdisziplinäre Gebirgsforschung der Österreichischen Akademie der  
748 Wissenschaften, Innsbruck, PANGAEA, <https://doi.org/10.1594/PANGAEA.818772>, 2016.

749  
750 Fischer, A., Fickert, T., Schwaizer, G., Patzelt, G. and Groß, G.: Vegetation dynamics in Alpine glacier forelands tackled  
751 from space, *Scientific reports*, 9(1), pp.1-13, 2019.



752  
753 ~~Fischer, A., Seiser, B., and Stoeker-Waldhuber, M.: Capturing deglaciation in the Austrian Silvretta: Methods and~~  
754 ~~Results, in review.~~  
755  
756 Gabbi, J., Huss, M., Bauder, A., Cao, F., & Schwikowski, M.: The impact of Saharan dust and black carbon on albedo  
757 and long-term mass balance of an Alpine glacier, *The Cryosphere*, 9(4), 1385-1400, 2015.  
758  
759 Gardner, A. S. and Sharp, M. J.: A review of snow and ice albedo and the development of a new physically based  
760 broadband albedo parameterization, *Journal of Geophysical Research: Earth Surface*, 115(F1), 2010.  
761  
762 GeoPandas developers: GeoPandas 0.8.0. URL: <https://geopandas.org/>, 2013-2019. Accessed: 2020.  
763  
764 Gillies, S., & others. (n.d.). Rasterio: Geospatial raster i/o for Python programmers. Mapbox, 2013. Retrieved from  
765 <https://github.com/mapbox/rasterio>, 2020.  
766  
767 Gorelick, N., Hancher, M., Dixon, M., Ilyushchenko, S., Thau, D., and Moore, R.: Google Earth Engine: Planetary-scale  
768 geospatial analysis for everyone, *Remote Sensing of Environment*, 202, pp.18-27, 2017.  
769  
770 Greuell, W. and de Wildt, M.D.R.: Anisotropic reflection by melting glacier ice: Measurements and parametrizations in  
771 Landsat TM bands 2 and 4. *Remote Sensing of Environment*, 70(3), pp.265-277, 1999.  
772  
773 Hall, D. K., Chang, A. T. C., Foster, J. L., Benson, C. S., and Kovalick, W. M.: Comparison of in situ and Landsat  
774 derived reflectance of Alaskan glaciers, *Remote Sensing of Environment*, 28, 23-31, 1989.  
775  
776 Hall, D. K., Bindschadler, R. A., Foster, J. L., Chang, A. T. C., and Siddalingaiah, H.: Comparison of in situ and  
777 satellite-derived reflectances of Forbindels Glacier, Greenland, *Remote Sensing*, 11(3), 493-504, 1990.  
778  
779 Hall, D.: *Remote sensing of ice and snow*, Springer Netherlands, 2012.  
780  
781 Henderson-Sellers, A. and Wilson, M.F.: Surface albedo data for climatic modeling. *Reviews of Geophysics*, 21(8),  
782 pp.1743-1778, 1983.  
783  
784 Hendriksa J, Pellikkaa P, Peltoniemi J. Estimation of anisotropic radiance from a glacier surface-Ground based  
785 spectrometer measurements and satellite-derived reflectances. In *Proceedings, 30th International Symposium on*  
786 *Remote Sensing of Environment: Information for Risk Management and Sustainable Development*, November 10-14,  
787 Honolulu, Hawaii, 2003.  
788  
789 Hoinkes, H., and Wendler, G.: Der Anteil der Strahlung an der Ablation von Hintereis- und Kesselwandferner (Ötztaler  
790 Alpen, Tirol) im Sommer 1958, *Archiv für Meteorologie, Geophysik und Bioklimatologie, Serie B*, 16(2-3), 195-236,  
791 1968.  
792  
793 Hunter, J.D.: Matplotlib: A 2D Graphics Environment, *Computing in Science & Engineering*, 9, 90-95, 2007.  
794  
795 Jaffé, A.: Über Strahlungseigenschaften des Gletschereises, *Archiv für Meteorologie, Geophysik und Bioklimatologie,*  
796 *Serie B*, 10(3), pp.376-395, 1960.  
797  
798 Kääb, A., Winsvold, S.H., Altena, B., Nuth, C., Nagler, T. and Wuite, J.: Glacier remote sensing using Sentinel-2. part I:  
799 Radiometric and geometric performance, and application to ice velocity. *Remote Sensing*, 8(7), p.598, 2016.  
800  
801 Klok, E.L., Greuell, W. and Oerlemans, J.: Temporal and spatial variation of the surface albedo of Morteratschgletscher,  
802 Switzerland, as derived from 12 Landsat images. *Journal of Glaciology*, 49(167), pp.491-502, 2003.  
803  
804 Knap, W. H., Brock, B. W., Oerlemans, J., and Willis, I. C.: Comparison of Landsat TM-derived and ground-based  
805 albedos of Haut Glacier d'Arolla, Switzerland, *International Journal of Remote Sensing*, 20(17), 3293-3310, 1999.  
806  
807 Koelemeijer, R., Oerlemans, J., and Tjemkes, S.: Surface reflectance of Hintereisferner, Austria, from Landsat 5 TM  
808 imagery, *Annals of Glaciology*, 17, 17-22, 1993.  
809  
810 Kuhn, M.: The response of the equilibrium line altitude to climate fluctuations: theory and observations, in: *Glacier*  
811 *fluctuations and climatic change*, 407-417, Springer, Dordrecht, 1989.  
812  
813 Lee, Y.: SpecDAL Reference. <https://specdal.readthedocs.io/en/latest/>, 2017. Accessed: September 2019.

807 Li, Z., Erb, A., Sun, Q., Liu, Y., Shuai, Y., Wang, Z., Boucher, P. and Schaaf, C.: Preliminary assessment of 20-m  
808 surface albedo retrievals from sentinel-2A surface reflectance and MODIS/VIIRS surface anisotropy measures. *Remote*  
809 *sensing of environment*, 217, pp.352-365, 2018.

810 Malinka, A., Zege, E., Heygster, G. and Istomina, L.: Reflective properties of white sea ice and snow. *The Cryosphere*,  
811 10, 2541–2557, 2016.

812  
813 Mayer, B. and Kylling, A.: Technical note: The libRadtran software package for radiative transfer calculations -  
814 description and examples of use, *Atmos. Chem. Phys.*, 5, 1855-1877, <https://doi.org/10.5194/acp-5-1855-2005>, 2005.

815  
816 Main-Knorn, M., Pflug, B., Louis, J., Debaecker, V., Müller-Wilm, U., and Gascon, F.: Sen2Cor for Sentinel-2, in:  
817 *Image and Signal Processing for Remote Sensing XXIII*, International Society for Optics and Photonics, Warsaw,  
818 Poland, 11-13 September 2017, Vol. 10427, p. 1042704, 2017.

819  
820 McKinney W.: Data structures for statistical computing in python. In: *Proceedings of the 9th Python in Science*  
821 *Conference 2010 Jun 28 (Vol. 445, pp. 51-56)*.

822  
823 Nicholson, L. and Benn, D.I.: Properties of natural supraglacial debris in relation to modelling sub-debris ice ablation.  
824 *Earth Surface Processes and Landforms*, 38(5), pp. 490-501, 2012.

825  
826 Di Mauro, B., Baccolo, G., Garzonio, R., Giardino, C., Massabò, D., Piazzalunga, A., Rossini, M., and Colombo, R.:  
827 Impact of impurities and cryoconite on the optical properties of the Morteratsch Glacier (Swiss Alps), *The Cryosphere*,  
828 11(6), 2393, 2017.

829  
830 Di Mauro, B., Garzonio, R., Baccolo, G., Franzetti, A., Pittino, F., Leoni, B., Remias, D., Colombo, R. and Rossini, M.:  
831 Glacier algae foster ice-albedo feedback in the European Alps. *Scientific reports*, 10(1), pp.1-9, 2020.

832  
833 Ming, J., Du, Z., Xiao, C., Xu, X., and Zhang, D.: Darkening of the mid-Himalaya glaciers since 2000 and the potential  
834 causes, *Environmental Research Letters*, 7(1), 014021, 2012.

835  
836 Ming, J., Wang, Y., Du, Z., Zhang, T., Guo, W., Xiao, C., Xu, X., Ding, M., Zhang, D., and Yang, W.: Widespread  
837 albedo decreasing and induced melting of Himalayan snow and ice in the early 21st century, *PLoS One*, 10(6),  
838 e0126235, 2015.

839  
840 Moller, M. and Moller, R.: Modeling glacier-surface albedo across Svalbard for the 1979–2015 period: The  
841 HiRSvC500-a data set. *J. Adv. Model. Earth Syst.*, 9, 404– 422, 2017.

842  
843 Naegeli, K., Damm, A., Huss, M., Schaepman, M., and Hoelzle, M.: Imaging spectroscopy to assess the composition of  
844 ice surface materials and their impact on glacier mass balance, *Remote Sensing of Environment*, 168, 388-402, 2015.

845  
846 Naegeli, K. and Huss, M.: Mass balance sensitivity of mountain glaciers to changes in bare-ice albedo. *Annals of*  
847 *Glaciology*, No. 75, *The Cryosphere in a Changing Climate*, 2017.

848  
849 Naegeli, K., Damm, A., Huss, M., Wulf, H., Schaepman, M., and Hoelzle, M.: Cross-Comparison of albedo products for  
850 glacier surfaces derived from airborne and satellite (Sentinel-2 and Landsat 8) optical data, *Remote Sensing*, 9(2), 110,  
851 2017.

852  
853 Naegeli, K., Huss, M. and Hoelzle, M.: Change detection of bare-ice albedo in the Swiss Alps, *The Cryosphere*, 13(1),  
854 397-412, 2019.

855  
856 Nicodemus, F.E., Richmond, J.C., Hsia, J.J., Ginsberg, I.W. and Limperis, T.: Geometrical considerations and  
857 nomenclature for reflectance, Vol. 160. Washington, DC: US Department of Commerce, National Bureau of Standards,  
858 1977.

859  
860 Oerlemans, J.: *Glaciers and climate change*. CRC Press, 2001.

861  
862 Oerlemans, J., R. H. Giesen, and M. R. Van den Broeke: Retreating alpine glaciers: increased melt rates due to  
863 accumulation of dust (Vadret da Morteratsch, Switzerland), *Journal of Glaciology*, 55, no. 192, 729-736, 2009.

864  
865 Painter, T. H., Flanner, M. G., Kaser, G., Marzeion, B., VanCuren, R. A., and Abdalati, W.: End of the Little Ice Age in  
the Alps forced by industrial black carbon, *Proceedings of the National Academy of Sciences*, 110(38), 15216-15221,  
2013.

866  
867 Pandzić, M., Mihajlović, D., Pandzić, J. and Pfeifer, N.: Assessment of the geometric quality of sentinel-2 data. In  
868 XXIII ISPRS Congress, Commission I, Vol. 41, No. B1, 489-494. International Society for Photogrammetry and  
869 Remote Sensing, 2016.

870 Paul, F., Machguth, H., and Käab, A.: On the impact of glacier albedo under conditions of extreme glacier melt: the  
871 summer of 2003 in the Alps, *EARSeL eProceedings*, 4(2), 139-149, 2005.

872 Qu, B., Ming, J., Kang, S. C., Zhang, G. S., Li, Y. W., Li, C. D., Zhao, S.Y., Ji, Z. M., and Cao, J. J.: The decreasing  
873 albedo of the Zhadang glacier on western Nyainqentanglha and the role of light-absorbing impurities, *Atmospheric  
874 Chemistry and Physics*, 14(20), 11117-11128, 2014.

875  
876 Richter, R. and Schläpfer, D.: *Atmospheric/Topographic Correction for Satellite Imagery: ATCOR-2/3 UserGuide"*,  
877 DLR IB 565-01/11, Wessling, Germany, 2011.

878  
879 Rhodes, B.: PyEphem. URL: <https://rhodesmill.org/pyephem/toc.html>, 2020.

880  
881 Sauberer, F.: Versuche über spektrale Messungen der Strahlungseigenschaften von Schnee und Eis mit Photoelementen,  
882 *Meteorol. Z.*, 55, 250, 1938.

883  
884 Sauberer, F. and Dirmhirn, I.: Untersuchungen über die Strahlungsverhältnisse auf den Alpengletschern, *Archiv Met.  
885 Geoph. Biokl. Ser. B.3*, 256, 1951.

886  
887 Sauberer, F. And Dirmhirn, I.: Der Strahlungshaushalt horizontaler Gletscherflächen auf dem Hohen Sonnblick, *Geogr.  
888 Ann.*, 34, 261, 1952.

889  
890 Schaepman-Strub, G., T. Painter, S. Huber, S. Dangel, M. E. Schaepman, J. Martonchik, and F. Berendse.: About the  
891 importance of the definition of reflectance quantities-results of case studies. In: *Proceedings of the XXth ISPRS  
892 Congress*, 361-366, 2004.

893  
894 Schaepman-Strub, G., Schaepman, M. E., Painter, T. H., Dangel, S., and Martonchik, J. V.: Reflectance quantities in  
895 optical remote sensing—Definitions and case studies. *Remote sensing of environment*, 103(1), 27-42, 2006.

896  
897 Shuai, Y., Masek, J.G., Gao, F. and Schaaf, C.B.: An algorithm for the retrieval of 30-m snow-free albedo from Landsat  
898 surface reflectance and MODIS BRDF. *Remote Sensing of Environment*, 115(9), 2204-2216, 2011.

899  
900 Storey, J., Choate, M. and Lee, K.: Landsat 8 Operational Land Imager on-orbit geometric calibration and performance.  
901 *Remote sensing*, 6(11), 11127-11152, 2014.

902  
903 U.S. Geological Survey: Landsat 8 Collection 1 (C1) Land Surface Reflectance Code (LaSRC) Product Guide Version  
904 3.0, 2020. <https://www.usgs.gov/media/files/landsat-8-collection-1-land-surface-reflectance-code-product-guide>  
905 Accessed: September 17, 2020.

906  
907 van As, D., Fausto, R. S., Colgan, W.T., and Box, J.E.: Darkening of the Greenland ice sheet due to the melt albedo  
908 feedback observed at PROMICE weather stations. *Geological Survey of Denmark and Greenland (GEUS) Bulletin*  
909 28:69-72, 2013.

910  
911 Van de Wal, R.S.W., Oerlemans, J., and Van der Hage, J.C.: A study of ablation variations on the tongue of  
912 Hintereisferner, Austrian Alps, *Journal of Glaciology*, 38(130), pp.319-324, 1992.

913  
914 Van der Walt, S., Colbert, C., and Varoquaux, G.: The NumPy Array: A Structure for Efficient Numerical Computation,  
915 *Computing in Science & Engineering*, 13, 22-30, 2011.

916  
917 Van Rossum, G., Drake, F.L.: *Python 3 Reference Manual*. Scotts Valley, CA: CreateSpace; 2009.

918  
919 Vermote, E., Justice, C., Claverie, M., and Franch, B.: Preliminary analysis of the performance of the Landsat 8/OLI  
920 land surface reflectance product, *Remote Sensing of Environment*, 185, 46-56, 2016.

921  
922 Winther, J. G.: Landsat TM derived and in situ summer reflectance of glaciers in Svalbard, *Polar Research*, 12(1), 37-55,  
923 1993.

923  
924 Wu, X., Wen, J., Xiao, Q., You, D., Lin, X., Wu, S. and Zhong, S.: Impacts and Contributors of Representativeness

- 924 Errors of In Situ Albedo Measurements for the Validation of Remote Sensing Products. IEEE Transactions on  
925 Geoscience and Remote Sensing, 57(12), 9740-9755, 2019
- 926 Zemp, M., Frey, H., Gärtner-Roer, I., Nussbaumer, S.U., Hoelzle, M., Paul, F., Haeberli, W., Denzinger, F., Ahlstrøm,  
927 A.P., Anderson, B., and Bajracharya, S.: Historically unprecedented global glacier decline in the early 21<sup>st</sup> century,  
928 Journal of Glaciology, 61(228), 745-762, 2015.
- 929 Zemp, M., Huss, M., Thibert, E., Eckert, N., McNabb, R., Huber, J., Barandun, M., Machguth, H., Nussbaumer, S.U.,  
930 Gärtner-Roer, I. and Thomson, L.: Global glacier mass changes and their contributions to sea-level rise from 1961 to  
931 2016, Nature, 568(7752), 382-386, 2019.
- 932 Zeng, Q., Cao, M., Feng, X., Liang, F., Chen, X., and Sheng, W.: A study of spectral reflection characteristics for snow,  
933 ice and water in the north of China, Hydrological applications of remote sensing and remote data transmission, 145,  
934 451-462, 1984.
- 935